國立清華大學

博士論文

National Tsing Hua University

Ph.D Thesis

Thrombospondin Type I Domain Containing 7A
參與血管新生中內皮細胞遷移的功能分析

The Functional Analysis of Thrombospondin Type I Domain Containing 7A in Vascular Endothelial Cell Migration during Angiogenesis

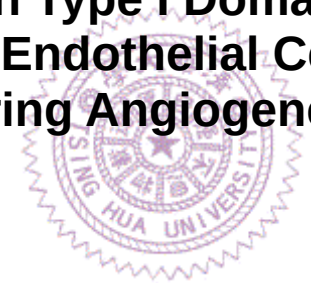

系　　所：生物資訊與結構生物研究所

學　　號：**944201**

姓　　名：王捷暉 **(Chieh-Huei Wang)**

指導教授：莊永仁 博士 **(Dr. Yung-Jen Chuang)**

中華民國一百年四月

April 2011

Contents

TSING HUA UNIVERSITY

List of Tables

List of Figures

Acknowledge

I would like to thank my mentor Dr. Yung-Jen Chuang, who initially began the project and guided me with extraordinary enthusiasm and patience. I would also like to acknowledge my committee members Dr. Bon-Chu Chung, Dr. Yun-Jin Jiang, Dr. Chiou-Hwa Yuh, and Dr. Chie-Pein Chen for their time and recommendations for this thesis. In addition, I would like to extend a special thank to Dr. Steven D. Leach, Dr. Shu Liu, and Dr. Lawrence L. Leung for their instructions during my graduation education.

I would like to thank my lab members I-Hui Chen, Meng-Wei Kuo, Hau-Shien Chan, Chian-Huei Wang, Pei-Tsu Su, Chun-Cheih Chao, Wei-Chang Huang, Zih-Yin Lai, and all other colleagues and alumni for their help during my stay in the lab. Finally, I am honored to inscribe my family in this thesis, Chi-Chen Wang, Yen-Chun Wang, and Szu-Han Wang for their wholehearted supports in my life. This thesis is all to my Father Chi-Chen Wang who left us by the end of 2010.

Abstract

Angiogenesis is a highly organized process under the control of guidance cues that direct endothelial cell (EC) migration, proliferation and differentiation. Recently, many molecules that were initially described as regulators of neural guidance were subsequently shown to also direct EC migration during angiogenesis. Here we report a novel protein, Thrombospondin-type I Domain-containing Protein 7A (THSD7A), which is required for EC migration and involved in the vascular patterning during development.

Identified by SAGE (serial analysis of gene expression) database mining and immunohistochemistry, THSD7A is highly expressed in human placenta vasculatures. To determine the function of THSD7A, we altered endogenous THSD7A expression in human umbilical vein endothelial cells (HUVECs) for subsequent angiogenesis assays. Our data indicated that downregulation of THSD7A in HUVECs enhanced cell migration and promoted tube formation, while overexpression of a THSD7A carboxyl-terminal fragment inhibited HUVEC migration and disrupted tube formation. Immunohistological analysis revealed that THSD7A was expressed at the leading edge of migrating HUVECs, and it co-localized with $\alpha_V\beta_3$ integrin and paxillin. This distribution was dispersed from focal adhesions after disruption of the actin cytoskeleton, suggesting the involvement of THSD7A in $\alpha_V\beta_3$ integrin and paxillin that mediates cytoskeletal reorganization during directed EC migration.

To characterize THSD7A in vivo, we performed whole-mount *in-situ* hybridization to reveal the spatiotemporal expression of *THSD7A* orthologue during zebrafish embryonic development, by which we detected zebrafish

thsd7a transcripts in the central nervous system. Notably, this expression exhibited a unique pattern along the ventral edge of neural tube, correlating with the growth path of angiogenic intersegmental vessels (ISVs). Antisense oligonucleotide-mediated gene knockdown of Thsd7a caused a lateral deviation of angiogenic ECs below the *thsd7a*-expressing sites, resulting in aberrant ISV patterning.

Collectively, our study revealed that THSD7A mediates angiogenic EC migration via cytoskeletal reorganization, and that zebrafish Thsd7a is a neural protein required for ISV angiogenesis during development. Future analysis on this novel protein shall provide a new perspective on the underlying mechanisms of directed EC migration, and shed light on the complex communication network between the nervous and vascular systems.

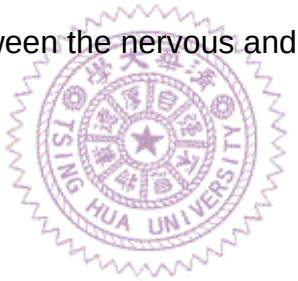

Abstract in Chinese 中文摘要

血管新生是一個高度組織化的過程，包括血管內皮細胞的遷移，複製與分化，並受各類誘導分子調控。近年來，許多參與神經系統發育的分子，亦被發現擁有調控血管內皮細胞遷移的能力，並參與血管新生的過程。本論文研究一新穎蛋白質，Thrombospondin-type I domain-containing protein 7A (THSD7A)。從實驗結果發現，此新穎蛋白質 THSD7A 可調控血管內皮細胞的遷移與形成管狀構造的能力，並參與神經與血管交互作用的發育過程。

由基因表現系列分析 (serial analysis of gene expression) 資料庫與組織染色結果中發現，THSD7A 高度表現於人類胎盤血管壁組織與臍帶靜脈內皮細胞 (Human Umbilical Vein Endothelial Cell; HUVEC)。為了進一步了解其功能，我在人類臍帶靜脈內皮細胞內改變 THSD7A 的表現，並觀察此對血管新生的影響。實驗數據顯示，抑制 THSD7A 可提高 HUVEC 遷移的能力，並促進其管狀結構的形成。另一方面，當超量表現 THSD7A 3’端保守片段於 HUVEC 中時，可抑制其遷移與形成管狀結構的能力。我們進一步利用免疫染色分析，定位出 THSD7A 表現分佈於遷移中細胞的最前端，並與細胞骨架分子$\alpha_v\beta_3$ integrin 和 paxillin 共位。而當細胞骨架被破壞時，亦可改變 THSD7A 於細胞內的分佈。此結果指出，THSD7A 可能透過$\alpha_v\beta_3$ integrin 和 paxillin 參與細胞骨架的組織重組，而進一步調控血管內皮細胞的遷移。

為了研究 THSD7A 在活體內的特性，我們利用全胚胎原位雜交法 (whole mount *in-situ* hybridization)偵測其於斑馬魚發育過程中的表現時間與位置。不同於人類胎盤血管系統的表現，斑馬魚 *thsd7a* 高量表達於發育中的中央神經系統，並沿神經管腹側形成一特殊的表現式樣。此特殊的表現位置正座落於斑馬魚體節血管新生至神經系統的路徑上。利用嗎啉反義核苷酸介導的基因剔除技術抑制 Thsd7a 的蛋白質表達，可造成遷移中的內皮細胞偏軌，破壞體節血管新生的典型樣式。

綜合本論文數據結果，我們發現 THSD7A 可透過細胞骨架重組以調控血管內皮細胞的遷移，並於斑馬魚發育中，參與神經與血管的交互作用。本研究結果發表一新穎蛋白質以探討血管新生的分子機轉，並有助於釐清神經與血管交互作用的複雜機制。

Chapter 1/ Introduction

1.1 Introduction of angiogenesis

The vertebrate vascular system is composed of a highly organized network of arteries, veins, and capillaries that infiltrates virtually all body tissues and organs [1, 2]. During the initial vasculogenesis, differentiation of endothelial progenitor cells precedes development of the primary vascular plexus. The second phase, termed angiogenesis, is characterized as the formation of new vessels from the pre-existing plexus either by sprouting from parental vessels or by intussusceptions [3-5].

Sprouting angiogenesis occurs in an orderly series of events. It initiates with vasodilatation, a process that increases vascular permeability to allow extravasations of proteases that disassemble vessel walls and degrade the extracellular matrix, thereby allowing the emigration of vascular endothelial cells (ECs) from their resident site [4]. Under precise controls of growth factors and guidance cues, ECs proliferate and migrate toward distant sites, and proceed in coalescence with adjacent ECs to form a new lumen. Then the new vessels undergo reassembly through reconstitution of surrounding basal matrix and recruitment of accessory cells [4, 6]. On the other hand, intussusceptive angiogenesis is a reorganization of existing vessels. It is characterized by a central perforation created by the protrusion of opposing vascular walls into the capillary lumen, resulting in an interstitial pillar. This intraluminal pillar is then invaded by pericytes and myofibroblasts which lay down collagen to provide basic matrix for the newly formed vessel networks [5, 7]. Concurrent sprouting and intussusceptive angiogenesis are involved in not only the vascularization during development, but also wound healing, tissue

repair, as well as malignant tumor growth.

1.2 Molecular mechanisms underlying angiogenesis

Angiogenesis is controlled by a dynamic balance between pro- and anti-angiogenic factors, and involves a cascade of molecular events. The initial vasodilatation of sprouting angiogenesis is mediated by several pro-angiogenic factors, among which vascular endothelial growth factor (VEGF) plays a critical role. VEGF stimulates vasodilatation through Src Kinase pathway, and involves the redistribution of vascular endothelial cadherin (VE-cadherin) and platelet endothelial cell adhesion molecule 1 (PCAM-1) [4, 8]. In addition, vasodilatation is also mediated by endothelial nitric oxide synthase (eNOS), which acts through VEGF and Rac1-dependent pathway [9, 10]. The dissociation of ECs from their resident sites may require angiopoietin-2 and its cognate receptor, Tie2, an endothelial-specific tyrosine kinase receptor, to breaks interactions between ECs and the periendothelial cells, such as pericytes and smooth muscle cells.

The surrounding extracellular matrix is dissolved by several different proteolytic enzymes, among which matrix metalloproteinases (MMPs) play important roles. MMPs are a family of zinc-dependent proteases responsible for degradation of the basement membrane [11, 12]. Cleavage of collagen type I by MMP-2, MMP-9, MMP-13, and MMP-16 is required for EC invasion of the extracellular matrix [13]. Cleavage of collagen type IV by MMP-2 exposes a cryptic $\alpha_V\beta_3$-binding site that facilitates EC migration and promotes angiogenesis [14]. MT1-MMP is required during migration of ECs on diverse matrix components, including gelatin, fibronectin, vitronectin, collagen type I, and aggrecan [11, 15]. The matrix degradation is also mediated by other

molecules, such as plasminogen activator, chymase, and heparanase [4, 11]. The degradation process not only enables EC migration, but also releases growth factors that sequester within the surroundings. These growth factors include VEGF, basic fibroblast growth factor (bFGF), and transforming growth factor-β (TGF-β), by which couple with integrin-associated cytoskeletal signals to promote proliferation and direct migration of sprouting ECs under a precisely spatiotemporal control. Coalescence of ECs and the formation of a new lumen involve cytoskeletal signaling downstream of integrins, and depend on Rac1, Rho, and Cdc42 pathways [16, 17]. Reconstitution of newly formed vessels requires the recruitment of accessory cells. Angiopoietin-1 that activates its tyrosine receptor, Tie2, allows the release of recruiting signal, platelet derived growth factor (PDGF), from ECs for pericytes, mesenchymal cells, and smooth muscle cells [6, 18]. Besides, Angiopoietin-1/ Tie2 signal counteracts Src activation by VEGF, thereby stabilizes inter-endothelial cell adhesions [19]. Angiopoietin-1/Tie2 also maintains vascular quiescence by activating cell survival kinase, AKT, and inhibiting cell apoptosis factor, Foxo1 [19].

Molecular control of intussusceptive angiogenesis remains obscure, but probably involves interplay among several known factors. Particularly, the factors, which are up-regulated during intussusceptive angiogenesis, include angiopoietins, VEGF, and PDGF-B [7, 20, 21]. Mice deficient in Angiopoietin-1 failed to undergo angiogenic remodeling [22]. In contrast, overexpression of Angiopoietin-1 or Angiopoietin-1 in combination with VEGF in mice exhibited abundant small holes in the capillary meshes [7, 23]. Angiopoietin-2 and PDGF-B may mediate intussusceptive angiogenesis by recruitment of pericytes [7]. Application of PDGF-B promoted intussusceptive capillary growth in a chicken chorioallantoic membrane (CAM) assay [24]; while inhibition of PDGF-B

signaling blocked pericyte recruitment, leading to failure of intussusceptive angiogenesis during retina development [25]. Further studies are required to reveal the molecular mechanisms underlying intussusceptive angiogenesis.

1.3 Developmental angiogenesis of zebrafish intersegmental vessels

Zebrafish (*Danio rerio*) has emerged as a valuable model system for studying vertebrate development due to its rapid external development, high fecundity, and optical transparency of embryos. Additionally, many genetic techniques are available, including gene over-expression and knockdown, stable transgenesis by Tol2 transposon and mutated alleles by TILLING (Targeting Induced Local Lesions In Genomes) or ZFN (Zinc-Finger Nucleases) [26-29]. Zebrafish is ideal for studying angiogenesis *in vivo*, particularly for studying its intersegmental vessel (ISV) formation. Zebrafish ISV angiogenesis begins by 20 hours post- fertilization (hpf) when angiogenic ECs sprout from the dorsal aorta. These ECs migrate dorsally following somite boundary, laterally to the notochord, and fuse adjacently to form the dorsal longitudinal anastomotic vessel along the roof of the neural tube by 30 hpf [30, 31]. ISV angiogenesis is guided by specialized ECs termed ‘tip cells’ [32, 33]. Located at the migratory front of ISV sprouts, tip cells continuously extend and retract filopodia, which is a dynamic F-actin protrusion studded with various surface receptors. Tip cells use this filopodia to explore the surrounding microenvironment for guidance cues, and lead the directed EC migration during ISV angiogenesis [2, 30].

The correct ISV patterning depends on complex coordination among guidance molecules that control EC cell behavior during development. For example, VEGF forms as dorsoventral guidance gradient in the surrounding

microenvironment of sprouting ISVs, and provides both short-range and long-range of patterning cue to direct EC migration through binding of its EC receptors, Flk1, Flt1, and neuropilin-1 [34]. Semaphorin-plexin signaling is also crucial for ISV patterning. Semaphorin3A is expressed in the developing somites, but is excluded from intersomitic boundaries. Semaphorin3A inhibits migration of plexinD1-expressing ECs, which then restricts the sprouting ISVs to growth along somite boundary [35]. Another example is netrin-1, which is a secreted protein emerging from the neural keel and the horizontal myoseptum. Netrin-1 acts with its EC receptor unc5b for ISV patterning, and may prevent premature ISV branching to the neural keel and horizontal myoseptum at later developmental stages [36, 37].

1.4 Research aims

A novel endothelial protein, Thrombospondin Type I Domain Containing 7A (THSD7A), with preferential expression in human umbilical vein endothelial cells (HUVECs) was identified by SAGE database mining [38]. Previously, RT-qPCR showed that *THSD7A* transcript was differentially expressed in HUVECs over four other non-EC cell types, including epithelial cells, fibroblasts, smooth muscle cells and monocytes [38]. Additionally, northern blot analysis surveying 12 different human tissues revealed *THSD7A* transcript to be highly expressed in placenta, in which a primary 6.4 kb mRNA transcript was identified [38].

In this thesis study, we verified the selective expression of THSD7A in human placental vasculature and umbilical vein endothelium by immunohistochemistry and western blot analysis. We then showed the biological function of THSD7A in EC migration and tube formation by both

gain- and loss-of-function approaches. The subcellular distribution of THSD7A during EC migration was examined by immunostaining, and further characterized in association with cytoskeletal reorganization. To unravel the physiological role of THSD7A *in vivo*, we performed in-situ hybridization on both mouse and zebrafish embryos using probes against *THSD7A* orthologues. We applied morpholino to knockdown Thsd7a expression during zeberafish development, and examined its effect in embryonic sprouting angiogenesis. In this study, we provide the very first evidence to show the biological role of THSD7A in both in-vitro and in-vivo systems. Our findings could make a significant impact on angiogenesis research, and may provide a new direction for future studies in the field of vascular biology.

Chapter 2/ Materials and Methods

2.1 Ethics Statement

All of the animal-use protocols in this thesis were reviewed and approved by the Institutional Animal Care and Use Committee of National Tsing Hua University (IRB Approval NO. 09507).

2.2 Primary isolation and culture of Human Umbilical Vein Endothelial Cell

Human umbilical cords were obtained from the Hsinchu Mackay Memorial Hospital under IRB regulation. ECs were isolated from umbilical cords by collagenase perfusion through the vein as described [39]. Specifically, umbilical vein was first flushed with PBS to clear all blood clots, and flushed with air to empty the vein vessel. Diluted collagenase solution (1:10 dilution of stock in PBS) was infused into umbilical vein till the solution leaked out from the other end. The entire umbilical cord was then incubated in 42˚C PBS for 12 min. After that, quench medium (DMEM with 10% FBS) was infused into umbilical vein to eject the mix of collagenase solution and detached HUVECs. The cells were collected by centrifuge at 150 g for 5 min, and re-suspend in 3 ml of EC medium (M200 medium supplemented with 2% FBS, 3 ng/ml basic fibroblast growth factor, 10 μg/ml heparin, 1 μg/ml hydrocortisone, and 10 ng/ml epidermal growth factor; Invitrogen, Carlsbad, CA). HUVECs were cultured in 0.2% gelatin-coated flask and incubated in 37˚C with 5% CO2 in a humidified incubator. HUVECs were used between passages 2 and 5 in all the experiments.

2.3 Immunostaining

Immunohistochemistry was performed on 10-μm cryosections of human placenta and umbilical cord. Specimens were permeabilized with 0.3% Tween20/PBS for 10 min, blocked with 3% BSA/PBS for 2 hours, and followed by incubation at 4˚C for overnight with a rabbit polyclonal antibody against a synthesized peptide epitope of THSD7A carboxyl-terminal element (CNRLKPLTLAYDGDADM) and a mouse monoclonal antibody against PECAM-1(Abcam, Cambridge, MA). After washing three times with PBS, signals were detected and amplified by DyLight 488-conjugated goat anti-mouse antibody and DyLight 594-conjugated goat anti rabbit antibody (1: 500 dilution of stock in 3% BSA/PBS; Jackson ImmunoResearch, PA). For immunocytochemistry, HUVECs seeded on a 0.2% gelatin-coated glass cover slip were fixed with 4% paraformaldehyde and permeabilized with 0.1% Triton X-100/PBS. Cells were then blocked with 3% BSA/PBS and incubated with the THSD7A antibody and mouse monoclonal antibodies against integrin (1:200 dilution in 3% BSA/PBS; Chemicon, Temecula, CA) and paxillin (1:200 dilution in 3% BSA/PBS ; Abcam, Cambridge, MA) followed by DyLight 488-conjugated goat anti-mouse antibody (1:500 dilution in 3% BSA/PBS). Nuclei were stained with 4', 6-diamidino-2-phenylindole (DAPI; 1:1000 dilution) for 15 min. 10 μM of Cytochalasin D (Sigma-Aldrich, St. Louis, MO) was used to disrupt the actin cytoskeleton in HUVECs. All images were captured using a confocal microscope (LSM510 Meta, Zeiss).

2.4 Plasmid construction

The THSD7A coding sequence was isolated from human placental cDNA. The carboxyl-terminal fragment (CTF; putative peptide region of 906-1657) of

THSD7A was amplified using polymerase chain reaction (PCR) and primers containing XhoI and BamHI sites: 5'-ccctcgaggactgtcaattgaccagctggt; 5'-cgggatccttacatgtcggcatctccatca. The PCR reaction was set up with Pfx DNA polymerase (Invitrogen, Carlsbad, CA), and subjected to denature at 94˚C for 2 min. 35 cycles were performed as follow: denature at 94˚C for 15 sec; anneal at 62˚C for 30 sec; extend at 68˚C for 2.5 min. The product was subsequently cloned into the pEGFP-C3 expression vector (Clontech, Mountain View, CA), which enabled the generation of a recombinant THSD7A-CTF transcription product fused to the c-terminus of enhanced GFP (eGFP).

2.5 Plasmid transfection

HUVECs were transfected with 4 μg of relevant vectors using the jetPEI-HUVEC transfection reagent (Polyplus-transfection, Illkirch, France) according to the manufacturer's instructions with minor modifications. Specifically, $1.5X10^5$ of HUVECs were seeded in 0.2% gelatin-coated T12.5 flask the day before experiment, which allowed cells to reach 50-60% confluence at the time of transfection. Before transfection, cells were washed once with PBS, and incubated in 3 ml of transfection medium (M200 with 2% FBS). The cells were transfected with 100 μl of 150 mM NaCl solution which contained 4 μg of relevant vectors and 8 μl of jetPEI-HUVEC transfection reagent, and incubated for 6 hours at 37˚C with 5% CO2 in a humidified incubator. After that, the transfection medium was replaced by EC medium. The transfected cells were incubated for a further 24 hours before subsequent experiments.

2.6 shRNA Gene silencing

Gene silencing was performed using the GIPZ lentiviral shRNAmir system (Open Biosystems, Huntsville, AL). An RNAi probe cloned in a shRNAmir lentiviral vector was designed to target THSD7A using the RNAi consortium database. The antisense probe sequences were the following: probe 102387, 5′-TTTCTTAATAAGCTCGCGGGC-3′; probe 102391, 5′-TTACTACACAAGAAATGTTCC-3′; probe 102392, 5′-TAAGGTTAAAGGTTTCAGTCGG-3′. The lentivirus was produced using TLA-HEK293T cells and titered according to the manufacturer's protocol. Specifically, 5.5 X10^6 of TLA-HEK293T cells were plated onto a 100 mm culture dish the day before transfection. The cells were then transfected with 5 ml of serum-free DMEM medium containing 37.5 μg of shRNA plasmid and 187.5 μg of Arrest-In reagent, and incubated for 6 hours at 37˚C with 5% CO2 in a humidified incubator. Following the incubation, the transfection medium was replaced with 10 ml of DMEM containing 10% FBS. Lentivirus-containing supernatants were harvested by 72 hours post-transfection. Concentration of lentivirus stock was performed by ultracentrigue using SW28 tube at 23,000 rpm for 1.5 hours at 4˚C. HUVECs cultured in T-25 flasks were incubated to reach 40-50% confluence, and infected with the lentivirus using an MOI of 0.5 for 24 hours, at which point the medium was replaced with supplemented M200. Cells were incubated for a further 48 hours before subsequent experiments.

2.7 Migration assay

The migration ability of HUVECs was assessed by Transwell (BD Biosciences, San Jose, CA) with an 8-μm pore size filter. The filter surface was

coated with 0.2% gelatin for 60 minutes at 37˚C. 5X10^4 of HUVECs with the indicated treatments were suspended in 200 μl of supplemented M200 medium and loaded into each upper well. The chambers were incubated at 37˚C for 4 hours with 5% CO_2 to allow cells migrate to the lower surface. Afterward, all cells on the upper surface of the filter were cleaned off using cotton swabs. Cells that had migrated to the lower surface were fixed with methanol and stained using DAPI for 15 min (1: 1000 dilution in methanol; Sigma-Aldrich, St. Louis, MO). The stained cells were imaged using an inverted fluorescence microscope (TE2000E, Nikon, Kanagawa, Japan) with a cooled CCD (Evolution VF, MediaCybernetics, Bethesda, MD) and processed using the program Extended Depth of Field in the Image-pro plus AMS software (MediaCybernetics, Bethesda, MD). Stained cells were counted in five random fields at 200X magnification. Migration rate was calculated as the number of migrated cells normalized to empty-vector controls. Each experiment was performed in triplicate and repeated at least three times.

2.8 Tube formation assay

Basement membrane matrix (BD Biosciences, San Jose, CA) was thawed at 4˚C, used to coat each well of a 48-well plate, and allowed to polymerize at 37˚C for 30 minutes. HUVECs (2.4 X10^4 cells/200 μl) with the indicated treatment were suspended in supplemented M200 medium and plated on matrigel-coated wells for 5 hours at 37˚C with 5% CO_2. Images were captured and processed as described above. Tube length was measured by Image-pro plus AMS software (MediaCybernetics, Bethesda, MD), and quantified in five random fields at 40X magnification. Each sample was assayed in triplicate and repeated at least three times.

2.9 Cloning of zebrafish Thsd7a ortholog

The reference sequence of zebrafish *thsd7a* was retrieved from the Vertebrate Genome Annotation database, amplified by PCR using primers 5'-ATCGATCCATGGGGAAGGTGTATGG-3' and 5'-CTCGAGCTACATGTCAGCATCGCCG-3'. The PCR setup was being with Pfx DNA polymerase (Invitrogen, Carlsbad, CA). After denature at 94˚C for 2 min, 35 cycles of reaction was performed as follow: denature at 94˚C for 15 sec; Anneal at 60˚C for 30 sec; Extend at 68˚C for 5 min. The product was then cloned into the pGEMTeasy vector (Promega, San Luis Obispo, CA) and the $pCS2^{+}$ vector (Addgene, Cambridge, MA). The cloning sequence was verified by directly sequencing, and deposited in GenBank database (GenBank accession number: HQ267705)

TSING HUA UNIVERSITY

2.10 Phylogenetic analysis

Phylogenetic analysis of Thsd7a orthologs in different species was performed by MEGA4 software [40], using the neighbor-joining method with referencing to human THSD7B and zebrafish Thsd7b. Identical in-group topologies were also obtained from the maximum-parsimony and maximum-likelihood methods. Bootstrap was set as 1000 replicates.

2.11 Whole-mount *in situ* hybridization (ISH)

An antisense probe against zebrafish *thsd7a* transcript was amplified by PCR using primers 5'- TGTGAAGTGAGCGAGTGGTC-3' and 5'-TAGCTGGGTGGTGTTATGAGGA-3', cloned into the pGEMTeasy vector (Promega, San Luis Obispo, CA), and synthesized by SP6 polymerase with DIG-labeled UTP. Embryos were fixed in 4% paraformaldehyde and stored at

-20˚C in methanol for up to six months. After serial rehydration to 100% PBST, embryos were permeabilized by proteinase K at 28˚C (stock 20 mg/ml; 1:1000-2000 diluted down in PBST based on age) and re-fixed in 4% paraformaldehyde for 20 min at R.T. Afterward, embryos were pre-hybridized in hybridization buffer (Hyb; 50% Formamide; 5X sodium citrate buffer; 0.1% Tween20; 50ug/ml of Heparin; 50ug/ml of Yeast tRNA; pH5.5) at 65˚C for 2-5 hours. Following the pre-hybridization, 100 ng of probe was added to embryos in Hyb overnight at 65˚C. Embryos were then washed with 75% Hyb, 50% Hyb, and 25% Hyb in 2 X sodium citrate buffer (SSC), then in 0.2X SSC for 1 hour. After blocking with 2% BSA in maleic acid buffer (100mM maleic acid; 150mM NaCl; 0.1% Tween20; pH7.5), an AP-conjugated anti-Dig antibody (1:8000 dilution in maleic acid buffer) was added and allowed to react with the NBT/BCIP substrate (Roche, Basel, Switzerland). In terms of fluorescent ISH, Embryos were fixed, stored, rehydrated, and hybridized with the probe as described above. After serially washing by Hyb/ SSC, embryos were blocked with 2X Roche blocking reagent. Signals were amplified by using a POD-conjugated anti-Dig antibody (1:1000 dilution in maleic acid buffer) and TSA-plus fluorescence kits (PerkinElmer, MA). To stain the vasculature, zebrafish embryos of the Tg(fli1:EGFP)^{y1} transgenic strain were stained with a rabbit polyclonal antibody against eGFP (1:500 dilution in maleic acid buffer; Novus Biologicals, Littleton, CO) and a DyLight 488-conjugated goat anti-rabbit antibody (1: 1000 dilution in maleic acid buffer; Jackson ImmunoResearch, PA). Images were captured using a stereomicroscope (SMZ1500; Nikon, Kanagawa, Japan) equipped with a CCD camera (DS-Fi1; Nikon, Kanagawa, Japan). Fluorescent signal was detected by using a confocal microscopy (A1R; Nikon, Kanagawa, Japan) and NIS-Elements

image software (Nikon, Kanagawa, Japan).

2.12 Alkaline phosphatase staining

Embryos were fixed in 4% paraformaldehyde at R.T. for 30 min, serially dehydrated in methanol, and stored at -20˚C for up to 6 months. After permeabilization with pre-cooled acetone at -20˚C for 30 min, embryos were then washed twice with PBST and equilibrated in NTMT buffer (0.1M Tris-HCl pH 9.5, 50mM MgCl, 0.1M NaCl, 0.1% tween20) for 15 min, three times. Endogenous alkaline phosphatase was stained for 15-30 min by using solution of 170 μg/ml of NBT and 87.5 μg/ml of BCIP in PBST. Reaction was stopped by adding 5% formamide and 10% hydrogen peroxide in PBST for 20 min, and washed with PBST three times.

2.13 Morpholino injection and mRNA rescue

Morpholino phosphorodiamidate oligonucleotides (morpholino, MO) were designed and synthesized by Gene Tools (Philomath, OR) to target splice junctions of the zebrafish *thsd7a* gene. The sequences were as follows (mismatched bases are underlined): MO1, 5’-TGTATGTTTTTACCCACCATGACTG-3’; 5-base mismatch control for MO1 (msMO1), 5’-TCTATCTTTTTAGCCACGATGAGTG-3’; MO2, 5’-GTGCCAGTTTTGTTACCGTCTTTGC-3’; 5-base mismatch control for MO2 (msMO2), 5’-GTCCCACTTTTCTTACGGTCTTTCC-3’. MOs were dissolved in nuclease-free water at a concentration of 1 mM and diluted in 1× Danieau solution with 0.05% phenolsulfonphthalein for injection of embryos at the 1-2 cell stage. Capped mRNA of *thsd7a* was synthesized using the mMESSAGE mMACHINE system (Ambion, Austin, TX) with SP6 RNA polymerase and

injected into 1-cell stage embryos. Fluorescent images were captured at 100× magnification using an inverted fluorescent microscope (TE2000E; Nikon, Kanagawa, Japan) with cooled CCD (Evolution VF; MediaCybernetics, Bethesda, MD). The images were processed using the Extended Depth of Field in Image-pro plus AMS software (MediaCybernetics, Bethesda, MD).

2.14 Microangiography

Microangiography was performed by injecting zebrafish embryos with 0.04 μm fluorescent carboxylated latex beads (red-orange fluorescent; Invitrogen, Carlsbad, CA). Embryos were anesthetized with tricaine (Sigma-Aldrich, St. Louis, MO) and embedded in 1% low-melting agarose. 4.6 nl of diluted fluorescent beads (1:1 of stock in 2% BSA) were then microinjected into the sinus venosus. Injected embryos were immediately imaged using an inverted fluorescent microscope (TE2000E; Nikon, Kanagawa, Japan) and Image-pro plus AMS software (MediaCybernetics, Bethesda, MD).

2.15 Real-time quantification polymerase chain reaction (RT-qPCR)

Real-time analysis was performed using an ABI PRIME7500 with Sequence Detection Software. 1 ug of total RNA was reverse-transcribed into cDNA using SUPERSCRIPT Ⅲ (Invitrogen, Carlsbad, CA). RT-qPCR reaction was prepared using SYBR Green Master Mix (Applied Biosystems, Carlsbad, CA) with the following primers: 5'-AAACGTGTCCTGCTTCGTGT-3' and 5'-CCACATCGTCCAGTCTGTCA-3'. Data were analyzed using ABI 7500 System SDS Software. All RT-qPCR products were cloned into pGEMTeasy vector (Promega, San Luis Obispo, CA) and sequenced.

2.16 Statistical analysis

Student's T-test (with two-tailed distribution and unequal variance) was performed in Microsoft Excel to test for differences between two sample populations.

Chapter 3

Thrombospondin Type I Domain Containing 7A (THSD7A) Mediates Endothelial Cell Migration and Tube Formation

3.1 *THSD7A* was identified as a novel EC-subtype gene

THSD7A cDNA contains an open reading frame of 4,971 nucleotides and encodes a hypothetical polypeptide of 1,657 amino acids. Sequence analysis predicted THSD7A contains an amino-terminal signal peptide (47 amino acids in length) followed by at least ten TSRs, one RGD site, six tryptophan-rich (WSXW) sequences, one CD36-binding motif, one putative transmembrane domain (spanning 24 amino acids), and a short cytoplasmic region (27 amino acids in length) (Fig. 1). This domain composition suggested that THSD7A may participate in angiogenesis through regulating EC migration. NCBI AceView Gene annotation predicted *THSD7A* produces nine different mRNAs, including seven alternatively spliced variants and two unspliced forms [41] (Fig. 2). Notably, it shows that 101 bp of *THSD7A* are antisense to the spliced gene rehiya, raising the possibility of regulated alternative transcription.

To verify this virtual prediction, immunohistochemical analysis was performed on placenta and umbilical cord using a specific antibody raised against the carboxyl-terminus of THSD7A. THSD7A expression was highly associated with platelet endothelial cell adhesion molecule (PECAM-1) in placental villi and endothelium (Fig. 3A-C). Its expression was also co-localized consistently with PECAM-1 in umbilical vein endothelium (Fig. 3D-F). Western blot analysis with HUVEC extracts revealed three bands with MWs of 100 KDa, 88 KDa, and 78 KDa (Fig. 4A), suggesting that there are three forms of THSD7A in HUVECs arising either from alternative splicing or

post-translational processing. Taken together, these findings demonstrate that THSD7A is prominently expressed in placental endothelium and HUVECs with at least three different variants.

3.2 THSD7A inhibited primary endothelial cell migration and tube formation *in vitro*

A previous report based on genome-wide yeast-two hybrid screening indicated that THSD7A interacts with paxillin-associated protein with ARFGAP activity 3 (PAG3) through its carboxyl-terminal region (putative peptide region of 1630-1657) [42]. Additionally, the seven alternatively spliced variants of *THSD7A* are predicted to have the same carboxyl terminus (Fig. 2), suggesting that a major functional domain of THSD7A resides in its carboxyl terminus. Consequently, a carboxyl-terminal fragment of THSD7A (THSD7A-CTF; putative peptide region of 906-1657) was cloned and fused with eGFP in the pEGFP-C3 vector, which was then transfected into HUVECs for functional assays. The amplified expression of THSD7A-CTF was verified by western blot (Fig. 4B).

Given THSD7A's endothelial specificity, its domain composition of multiple TSRs and the RGD motif in its amino acid sequence (Fig. 1), suggesting that THSD7A may play a role in EC migration during angiogenesis. The effect of THSD7A in EC migration was examined by using the transwell assay. Overexpression of eGFP-fused THSD7A-CTF in HUVECs reduced the cell migration rate by 36.4% compared to parental untreated cells or cells transfected with empty vector (Fig. 5A), supporting the hypothesis that THSD7A is engaged in the regulation of EC migration. To address this question further, a lentiviral infection approach was performed to introduce

short hairpin RNA (shRNA) to knock down endogenous THSD7A expression in HUVECs. Three shRNA antisense probes against different sites of THSD7A mRNA were tested. The knockdown efficacy was examined by RT-qPCR, and showed that probe 102392 had the most significant effect in down-regulating THSD7A expression in HUVECs (Fig. 6). Therefore this probe was chosen for all subsequent experiments. As expected, down-regulation of THSD7A led to a 2-fold increase in HUVEC motility compared to parental untreated cells or cells infected with non-silencing control virus (Fig. 5B).

The role of THSD7A in angiogenesis was further evaluated by a matrigel-induced tube formation assay. HUVECs with overexpressed THSD7A-CTF formed a fragmented structure, while control cells showed an organized tubular network (Fig.5C). Quantitative analysis indicated a significant 15.5% decrease in capillary tube length in THSD7A-CTF HUVECs as compared to the control. Conversely, THSD7A downregulation in HUVECs enhanced tubular network formation by 27.0% (Fig. 5D). Taken together, these gain- and loss-of-function experiments support a repressive role of THSD7A in EC migration and tube formation.

3.3 THSD7A was expressed in the leading edge of migrating HUVECs and joined the $\alpha_v\beta_3$-paxillin focal complex.

EC migration is essential to angiogenesis [43]. The effects of THSD7A inside HUVECs may act through focal adhesions, which with unique molecular composition offer many regulatory features in controlling cytoskeletal reorganization to direct EC migration [44, 45]. For example, the focal complexes that accumulate in the leading edge of migrating cells are enriched with $\alpha_V\beta_3$ integrin and paxillin, while contractile contacts that form fibrillar adhesions are

composed of $\alpha_5\beta_1$ integrin and tensin [46]. To investigate the underlying mechanism of THSD7A in EC migration, we performed immunocytochemistry to reveal the subcellular distribution of THSD7A in migrating HUVECs, and examined its association with cytoskeleton and focal complex molecules.

Confluent HUVECs on a culture dish were partially scraped away with a pipette tip to enable observation of the cells migrating into the unoccupied space. THSD7A expression was clearly detected at the extremities of the actin cytoskeleton in the leading edge of migrating HUVEC (Fig. 7A-D, indicated by the white arrows). This distribution suggests that THSD7A may be associated with the focal complex molecule, $\alpha_v\beta_3$ integrin, which accumulates in the leading membrane protrusions of migrating ECs [47]. As expected, THSD7A was found to co-localize with $\alpha_v\beta_3$ integrin in the focal complex, but not in the perinuclear zone (Fig. 7E-H), suggesting that THSD7A may elicit its repressor effect by masking the membrane-bound $\alpha_v\beta_3$ integrins and preventing them from interacting with extracellular signals. Furthermore, THSD7A contains an RGD motif, suggesting that THSD7A may be recognized by $\alpha_V\beta_3$ integrin through this RGD motif in mediating EC migration.

In addition, paxillin, an integrin-associated scaffold protein in focal adhesions, serves as a transacting adaptor between the extracellular matrix and intracellular signaling [48, 49]. Upon integrin activation by adhesion and growth factor stimulation, paxillin is recruited from the cytoplasmic pool to the focal adhesions, which is crucial to the assembly of integrins and other regulatory proteins that control the dynamics of cytoskeletal reorganization during cell migration. Co-localization between $\alpha_v\beta_3$ integrin and paxillin has been observed in ECs and extravillous trophoblast cells [50, 51]. THSD7A was also co-localized with paxillin in HUVECs (Fig. 7I-L). Taken together, these

findings suggest the clustering of THSD7A with $\alpha_V\beta_3$ integrin and paxillin at focal adhesions. Notably, cells with defects in paxillin's LD4 motif exhibit a higher rate of random cell motility and alteration of the actin cytoskeleton [52]. This result is reminiscent of our study showing that knockdown of THSD7A in HUVECs increased the rate of cell migration, suggesting that THSD7A may cooperate with the paxillin's LD4 motif to direct EC migration.

Furthermore, interaction of THSD7A with the actin network was examined by disrupting the actin cytoskeleton with cytochalasin D (CyD), which is an inhibitor of actin polymerization [53, 54]. As expected, dispersion of THSD7A from these focal adhesion sites was observed in CyD-treated HUVEC (Fig. 8). It is noted that THSD7A remained co-localization with actin in the perinuclear zone after cytoskeleton depolymerization (Fig. 8), which underscored the association of THSD7A with the actin cytoskeleton. Collectively, these results show that THSD7A may be involved in the $\alpha_v\beta_3$-paxillin focal complex and participates in the regulation of the actin cytoskeleton to mediate EC migration.

Chapter 4

Zebrafish Thsd7a is a Neural Protein Required for Angiogenic Patterning during Development

THSD7A is previously shown to highly express in human placental vasculature and HUVECs. Human THSD7A was found to mediate HUVEC migration and tube formation *in vitro*. Distribution of THSD7A protein is closely associated with the actin cytoskeleton at the leading edge of migrating HUVECs, and co-localizes with the $\alpha_v\beta_3$ integrin-paxillin focal adhesion complex. To characterize the physiological role of THSD7A *in vivo*, we cloned the zebrafish ortholog of *THSD7A* for further analysis.

4.1 THSD7A is conserved among vertebrates

To start a comparative analysis on zebrafish *thsd7a*, the human THSD7A amino acid sequence was used to blast the Vertebrate Genome Annotation (Vega) database to identify the corresponding zebrafish ortholog. A deduced amino acid sequence was hereby hit (Vega transcript ID: OTTDART00000018747). Multiple sequence alignments revealed a 67-68% identity at the protein level between this predicted zebrafish Thsd7a and its orthologs in human, mouse, and chicken (Fig. 9 A-B). Phylogenetic analysis showed that the predicted zebrafish Thsd7a protein was clustered with human THSD7A and other vertebrate orthologs in contrast with the paralogous Thsd7b (Fig. 9 C). Similar to human, *in silico* domain analysis further showed that zebrafish Thsd7a contains at least ten thrombospondin type-1 repeats (TSRs), five TGF-β-binding sites, one CD36-binding site, and a putative transmembrane domain (Fig. 9 A). The carboxyl-terminal portion of Thsd7A is

highly conserved, while more variation was detected among the orthologs in the amino-terminal region. Based on these analyses, the zebrafish *thsd7a* was successfully cloned into the pGEMTeasy vector. Notably, a two-amino acid insertion (Ala1059- Gln1060) was observed in the DNA sequencing results from three independent clones. These inserted amino acids were conserved among vertebrates but not present in the deduced sequence of zebrafish Thsd7a retrieved from the Vega database (Fig. 9 A, indicated by double underline).

4.2 The *thsd7a* transcripts were detected in the developing central nervous system in zebrafish and mouse embryos.

RT-qPCR was performed to reveal the temporal expression profile of *thsd7a* throughout embryonic development in zebrafish (Fig. 10). The *thsd7a* transcript could be detected in embryos at 2.25 hours post-fertilization (hpf), suggesting that *thsd7a* was provided maternally. The abundance of *thsd7a* transcript decreased gradually until 15 hpf, at which time zygotic *thsd7a* expression began to increase. The expression level then persistently increased throughout the examined developmental stages (Fig. 10). Next, the spatiotemporal expression pattern of *thsd7a* was examined in 15 to 48 hpf zebrafish embryos by whole-mount ISH (Fig. 11). The *thsd7a* transcripts were first detected in the dorsal region of embryos at 15 hpf (Fig. 11A). Notably, staining of *thsd7a* was over developed due to its low expression level at 15hpf (Fig. 10), resulting in weakly ubiquitous staining, that was most likely background signal when we compared to the control (Fig. 11B). By 22 and 32hpf (Fig.11C, F), *thsd7a* expression was clearly observed in the developing central nervous system (CNS). Interestingly, a unique expression pattern of

thsd7a was found along the ventral edge of neural tube (Fig. 11C, F; indicated by arrowheads). Higher-magnification images of embryos at 22 hpf were performed to show the specific expression of thsd7a in the neural tube (Fig. 11D), and that of the control embryo (Fig. 11E). A cross-section of the trunk region revealed that *thsd7a* was predominantly expressed at the edge of neural tube, and extended to the entire marginal zone of the spinal cord. (Fig. 11G). By 48 hpf, strong staining of *thsd7a* transcript was largely confined to the retina, cranial ganglia, pectoral fin, and central nervous system, including the midbrain, hindbrain, midbrain-hindbrain boundary, cerebellum, tectum, telencephalon, and spinal cord (Fig. 11H, I). To determine whether this expression pattern was conserved in mammalian development, a whole-mount ISH on E12.5 mouse embryos was performed, and showed that transcript staining of the mouse *Thsd7a* ortholog was prominently detected in the midbrain, hindbrain, neural tube, and segmented dorsal root ganglia (Fig. 12), with a pattern similar to that seen in zebrafish. Collectively, these data support conserved transcript expression of *Thsd7a* could be found in the developing CNS of the vertebrates.

4.3 Morpholino knockdown of Thsd7a in zebrafish embryos.

To further examine the role of Thsd7a in development, morpholino antisense oligonucleotides (MOs) was employed to inhibit the function of Thsd7a in zebrafish embryos. Two MOs with different targeting sites were used to disrupt *thsd7a* mRNA splicing. The first MO (MO1) blocked the third exon-intron boundary (Fig. 13A), whereas the second MO (MO2) targeted the twelfth splice junction (Fig. 13D). In addition, two 5-mismatched MOs were used as controls (msMO1; msMO2). MO efficacy was confirmed using reverse

transcription PCR. Injection of MO1 caused the third intron to be retained after splicing, leading to a reduced level of accurate mRNA transcription and decreased *thsd7a* expression in zebrafish embryos (Fig. 13B). In addition, RT-qPCR was conducted to quantify the knockdown level. Compared to the msMO1 control, it showed that the *thsd7a* mRNA level was reduced by 68.03% after injection of MO1 (Fig. 13C). On the other hand, injection of MO2 caused a complete deletion of the twelfth exon. A 712 bp fragment of *thsd7a* fragment was amplified in the cDNA pool derived from MO2-injected embryos, and a 977 bp *thsd7a* fragment was found from msMO2 controls (Fig. 13E). This result was consistent with the loss of exon 12, and was further confirmed by sequencing analysis.

4.4 Thsd7a is required for ISV angiogenesis during zebrafish development

Human THSD7A has been previously shown to mediate HUVEC migration and tube formation *in vitro* [55]. This finding prompted us to assess the potential role of Thsd7a in embryonic zebrafish angiogenesis.

Zebrafish ISV development occurs in a coordinated anterior-to-posterior progression [56, 57]. The antisense MOs was injected into Tg(fli1:EGFP)^{y1} transgenic zebrafish to facilitate observation of the knockdown effect on ISV angiogenesis through the fish's fluorescent vasculatures [58]. In non-injected embryos (data not shown) or embryos injected with msMO1 or msMO2, ISVs sprouted in an orderly fashion from the dorsal aorta at ~20 hpf, and progressed to the horizontal myoseptum. The sprouting ISVs then extended dorsally and fused adjacently to form the dorsal longitudinal anastomotic vessel along the dorsal roof of the neural tube around 29 hpf (Fig. 14A, C, E, G, I-K).

In embryos injected with MO1, the initial ISV sprouting was unaffected. However, instead of a full dorsal extension, the sprouting ISVs stalled at the horizontal myoseptum, right under where *thsd7a* was expressed, and deviated laterally to produce aberrant anastomoses. (Fig. 14B, F; indicated by white arrows). A close examination on the stalled vessels was conducted at different time points. In contrast to the normal ISV patterning seen in control siblings (Fig. 14I-K), the stalled ECs in the Thsd7a MO1-injected embryos exhibited abnormal tip cell-like membrane protrusions (Fig. 14L-N; indicated by white arrows). Interestingly, some laterally-deviated ECs generated a lamellipodia-like structure toward the neural tube (Fig. 14M-N; indicated by white arrowheads), suggesting an unpolarized migratory feature. Notably, embryos injected with a higher dose of MO1 (≥ 2 ng) exhibited a curved and shortened body axis with severe defects in ISV patterning, while the initial vessel sprouting was still unaffected (insets in Fig. 14B, F) It is also noted that few ISVs had reached the roof of the neural tube without following the prescribed orderly progression (Fig. 14F, H; indicated by white arrowheads) On the other hand, injection of MO2 resulted in ISV defects that were consistent to the MO1 results, indicating the specificity of the observed phenotype caused by Thsd7a knockdown (Fig. 14D, H). However, a higher dose of MO2 was required to detect this phenotype, possibly due to lower efficiency of MO2 to disrupt intact function of Thsd7a when the twelfth exon was deleted.

The spatial relationship between *thsd7a* expression in the neural tube and the growth paths of angiogenic ISVs was further examined by fluorescent ISH. Similar to the findings in the whole-mount ISH, the unique pattern of *thsd7a* transcript was detected in the ventral edge of the neural tube (Fig. 15A, D;

indicated by white arrows). Interestingly, this expression pattern coincided with the contact sites where angiogenic ECs migrate dorsally alongside the neural tube (Fig. 15C; indicated by white arrows). In the morphant, the stalled ECs produced extended membrane protrusions and deviated laterally to form the aberrant ISV pattern below the *thsd7a*-expressing sites (Fig. 15F; indicated by white arrowheads). These findings further underscore that Thsd7a was a neural molecule which could mediate polarized EC migration during ISV angiogenesis.

The penetrance of the MO-induced ISV defect was statistically evaluated. Both MO1 and MO2 injection led to aberrant ISV patterning in a dose-dependent manner (Table 1). It is observed that 50.39% (n = 382 from six independent experiments) and 49.30% (n = 500 from seven independent experiments) of embryos exhibited the described ISV defects after injection of 1 ng MO1 or 9 ng MO2, respectively. Injection of 2 ng MO1 or 18 ng MO2 led to ISV defects at frequencies of 68.03% (n = 135 from three independent experiments) and 60.45% (n = 169 from three independent experiments), respectively. The defective ISV phenotype could be partially rescued by injection of MOs in combination with *thsd7a* mRNA (Table 1). Co-injection of 1 ng MO1 and 0.8 ng *thsd7a* mRNA resulted in a penetrance of 34.83% (n= 246 from four independent experiments), which was significantly lower than that caused by injection of 1 ng MO1 alone ($p = 1.1\times10^{-5}$). Similarly, co-injection of 9 ng MO2 and 0.8 ng *thsd7a* mRNA reduced the defect penetrance from 49.30% to 24.51% (n = 159 from three independent experiments; $p = 7.38\times 10^{-5}$). While statistically significant, the incomplete rescue results most likely derive from the inability of ubiquitous mRNA overexpression to recapitulate the unique spatiotemporal expression pattern of *thsd7a in vivo.* This partial rescue

effect has been described in many other reports [59, 60].

4.5 Knockdown of Thsd7a impairs ISV angiogenic patterning

To further characterize the effect of Thsd7a knockdown on vascular patterning, ISV vascular network was examined in the control and morphant embryos at 50hpf. In contrast to the well-organized ISV patterning in the control siblings, the morphants displayed excessive abnormal ISV branching stemmed from the sprouting cells at the horizontal myoseptum (Fig. 16; indicated by white arrows), while some of the ISVs had reached the dorsal roof of the neural tube and formed dorsal longitudinal anastomotic vessel. It is observed that 56.19% of MO1 morphants (n = 119 from four independent experiments) displayed the abnormal ISV branching, and that 54.84% of MO2 morphants (n = 190 from three independent experiments) showed the defects (Table 2). On the other hand, by 50hpf, circulating erythrocytes were present in both morphants and control siblings. We observed that 80.36% (n = 119 from four independent experiments) and 70.41% (n = 96 from three independent experiments) of embryos exhibited normal blood circulation in the axial vasculature and the functional ISVs (Table 3). Collectively, these findings indicate that Thsd7a is required for ISV patterning, but does not affect functional vessels and hematopoiesis. Also, it shows that the observed ISV defects were not merely resulted from a developmental delay. Taken together, these data indicate that the neural Thsd7a plays a critical role in EC migration during ISV angiogenic patterning.

In previous study, human THSD7A was found prominently expressed in HUVECs over other non-EC cell types. It also suggested that THSD7A protein inhibited HUVEC migration and tube formation in a cell-autonomous manner.

However, in zebrafish embryos, Thsd7a was expressed in the neural tube and acted as a guidance molecule to control ISV angiogenesis. It suggests that Thsd7a functions non-autonomously in directing ISVs during zebrafish development. Also it implicates the different effects of zebrafish Thsd7a and human THSD7A in controlling migrated ECs may be regulated through different signaling pathways or additional cell-to-cell and cell-to-ECM interactions.

Interestingly, a soluble fragment of THSD7A was found in conditional medium when over-expressing full-length of human THSD7A in HEK293T cells. HUVEC treated with this conditional medium preferred forming tubes in a 3D-cultured system (Meng-Wei Kuo, unpublished). Accordingly, we proposed that a fragment of zebrafish Thsd7a may be released from neural cells, and forms a guidance gradient to direct EC migration during zebrafish ISV angiogenesis (Fig. 17). Many of these neural-secreted factors are shown to regulate angiogenesis [32]. For example, netrin-1a is a diffusible neural factor. Cooperated with its receptor UNC5B, netrin-1a was reported to mediate angiogenic EC navigation [36]. Interestingly, morpholino-knockdown of either netrin-1a or Unc5b in zebrafish embryos share similar phenotypes with Thsd7a morphant, i.e. lateral deviation of ISVs at the ventral edge of neural tube [36]. These findings suggest that Thsd7a may play an analogous role to that of netrin-1a-Unc5b signaling in regulating ISV angiogenesis.

Chapter 5/ Unpublished Data

5.1 THSD7A was involved in actin cytoskeletal reorganization in HUVECs.

Previously, THSD7A expression is shown to locate at the extremity of actin filaments at the leading edge of migrating HUVECs. In addition, THSD7A dispersed from the focal adhesion sites upon the disruption of actin organization. These findings suggest that THSD7A may regulate actin cytoskeletal reorganization in ECs. To address this issue, a lentiviral approach was performed to introduce a short hairpin RNA (shRNA) to knockdown THSD7A in HUVECs. While parental untreated cells or cells infected with non-silencing control virus displayed organized structure of actin cytoskeleton, 64.5% of HUVECs treated with THSD7A shRNA displayed abnormal accumulation of actin filaments at the plasma membrane, forming multiple membrane ruffles (Fig. 18). Notably, this abnormal ruffling is a characteristic of motile cells with a suppressed directed migration [52]. Taken together, these data supports the role of THSD7A in regulating actin cytoskeletal reorganization to direct EC migration during angiogenesis.

5.2 Other phenotypes in Thsd7a morphants

Other phenotypes in Thsd7a morphants were found, suggesting Thsd7a may play roles in other than ISV angiogenesis during zebrafish development. However, these phenotypes shall be carefully examined, and its incidents require further statistical analysis. For example, Knockdown of Thsd7a in zebrafish embryo caused developmental defects of aortic arches at 3 day post-fertilization (Fig. 19), and resulted in disconnection between aortic archs

and dorsal aorta as demonstrated by Alkaline phosphatase staining (Fig. 20; boxed region). Additionally, development of vasculature in embryonic eyes was disrupted (Fig. 20; indicated by arrowheads). These findings suggest that zebrafish Thsd7a may also be responsible for vascular development in head, particularly the vessels surrounding the CNS where *thsd7a* was expressed. Furthermore, while circulating erythrocytes were present in both morphants and control siblings, it is noted that this circulation follow the abnormal structure of ISVs in the Thsd7a morphant, when compared to the control that showed normal chevron-like pattern of ISV blood circulation. This finding suggests that Thsd7a affects the directed EC sprouting, but not on vessel lumenization during ISV development (Fig. 21). Besides, pericardial edema and enlarged heart were observed (Fig. 22). However, these two phenotypes were only found when embryos injected with morhpolino diluted in PBS, but not in Danieau solution. It was therefore most likely due to an unbalanced osmotic pressure caused by PBS injection.

It is interesting to note that TSRs have dual functions in both the vascular and nervous systems. For example, TSRs of Sema5 A regulate both EC migration and axon outgrowth [61-63]. Furthermore, *thsd7a* was expressed in the developing CNS. It raises a possibility that Thsd7a may enact roles not only in angiogenesis but also in neurogenesis, probably via its TSR domains. In this regard, even though the overall axonal projection of primary motoneruon was not significant affected in the Thsd7a morphants, we observed a retarded development of intraspinal neurons and highly branched motoneuron axons (Fig. 23). Additionally, it is found that zebrafish *thsd7a* expression pattern is similar to that of nestin, which is a pan marker of neural stem cells [64] (Fig. 24). On the other hand, while Northern blot analysis indicated that human *THSD7A*

was prominently expressed in placenta over other adult organs [38], it is noted that *THSD7A* transcript was detected in a relatively high level in the human fetal brain cDNA library (Fig. 25). Taken together, it implies that THSD7A may play important roles in the neurogenesis, probably through the regulation of neural stem cell development. In addition, interaction of α4 integrin-paxillin with coordinated activities of the Rho family of small GTPases is required to regulate neurite outgrowth[65, 66], implying the function of Thsd7a in regulating neuronal axons may also be achieved through paxillin, which is similar to that used in mediating human EC migration.

TSING HUA UNIVERSITY

Chapter 6/ Future Works

In summary, we showed that THSD7A is essential for EC migration during angiogenesis. To our knowledge, this work is the first report describing the biological functions and physiological characteristics of THSD7A. Further analysis of THSD7A should provide a new perspective on the underlying mechanisms of directed EC migration.

Clues to unravel the underlying mechanism may emerge from the findings that THSD7A was co-localized with $\alpha_V\beta_3$ integrin and paxillin in the focal complex. The role of $\alpha_V\beta_3$ integrin in angiogenesis remains controversial. Disruption of $\alpha_V\beta_3$ integrin can inhibit angiogenesis, supporting an inductive role of $\alpha_V\beta_3$ integrin in angiogenesis [67, 68]. In contrast, many persuasive studies reveal a repressive function of $\alpha_V\beta_3$ integrin in angiogenesis [67, 69, 70]. Therefore, it is possible that THSD7A may be involved in tilting the repressive effect of $\alpha_V\beta_3$ integrin to inhibit HUVEC migration and tube formation.

THSD7A has been previously shown to interact with PAG3 in a yeast-two-hybrid study [42]. PAG3 is a cytosolic ArfGAP protein that has GAP activity toward ADP ribosylation factors, including ARF1 and ARF5 *in vitro* and ARF6 *in vivo* [71, 72]. These ARF factors belong to small GTPases [73], and are important in the regulation of this paxillin recruitment [71, 74]. Interestingly, overexpression of PAG3 hampers cell migratory activity by hindering paxillin from being recruited to focal adhesions in an ARF6-associated manner [71]. In addition, THSD7A was detected at focal adhesions and the perinuclear area, in agreement with the known cellular distribution of PAG3 and paxillin [71]. Given the repressive effect of THSD7A in HUVEC migration, it suggests that THSD7A may function cooperatively with PAG3 and ARF family in

sequestering paxillin activity. Notably, ARF6 contributes to multiple membrane ruffles and coordinates with Rac1 and RhoA to regulate actin cytoskeleton reorganization[75]. Analysis of Rac1 or RhoA and the downstream factors, including Cdc42, FAK, Src, ERK1/2, PI3K, and Akt, is therefore important to assess the role of THSD7A in focal adhesion dynamics during cell migration. The possible interactions of THSD7A are summarized in Fig. 26, and remain to be verified.

THSD7A contains six WSXW motifs in its TSRs. These tryptophan-rich (WSXW) sequences are similar to those found in TSP1, which can bind to the latent TGF-β complex to instigate the TSP1-mediated conversion of TGF-β from its latent form to the active form [76]. It has also been documented that $\alpha_V\beta_3$ integrin is a receptor for TGF-β1 and TGF-β3 in mediating cell adhesion [77]. Additionally, paxillin and the actin cytoskeleton are rearranged upon treatment of ECs with TGF-β1 [78]. Taken together, these findings open the possibility that the effect of THSD7A in HUVEC migration is mediated by TGF-β, leading to the new hypothesis that THSD7A may inhibit the activation of TGF-β via these WSXW motifs and in turn block the signal transduction of the $\alpha_V\beta_3$-paxillin focal complex that directs EC migration.

On the other hand, the presence of a CD36-binding motif in THSD7A may provide an alternative mechanism. However, it is known that HUVECs do not express CD36 [79]. Therefore, the effects of THSD7A on HUVEC migration and tube formation are unlikely to be mediated via CD36 binding. Nevertheless, this raises the possibility that THSD7A may also elicit activity toward CD36-expressing cells in the microvasculature such as capillary sprout ECs.

During zebrafish development, *thsd7a* was expressed in the neural tube and required for ISV angiogenesis, suggesting that Thsd7a directed EC

migration in a non autonomous way. However, human THSD7A was expressed in both HUVECs and placental vasculature. Alternation of THSD7A expression in HUVECs affected cell migration and EC tubulogenesis *in vitro*. Whether Thsd7a acts primarily in neural or vascular cells is therefore not clear. Also, it is needed to directly demonstrate the cell-autonomy effect of zebrafish Thsd7a on ISV angiogenesis by either 1) transplantation experiments of morphant cells into wild type embryos (and all possible combinations), or 2) using a neural or vascular-specific promoter in DNA-based constructs to rescue the ISV defects. In addition, it is expected that mis-expressed Thsd7a in zebrafish would disrupt the ISV patterning.

Underlying mechanism of Thsd7a in directing EC migration during ISV angiogenesis remains obscure. To address this issue, it may begin by examining whether VEGF expression changes in the Thsd7a morphants. Besides, Notch signaling is involved in the process of specification of EC identity, position and behavior during ISV angiogenesis [80]. One could examine the role of Thsd7a in Notch pathway by coinjection Thsd7a Morpholino with rbpsuh morpholino (inhibit notch downstream factor) or with DAPT (chemical inhibitor of Notch signaling). Besides, VEGF receptor 3 (alternative name, Flt4) is involved in both VEGF and Notch signaling to direct EC tip cell migration [80, 81]. By ISH to reveal *flt4* expression change in the Thsd7a morphant, it may open the possibility to unravel the role of Thsd7a in directing EC migration through VEGF and/ or Notch pathways during ISV angiogenesis.

Given the new understanding on THSD7A provided by this study, several questions regarding the physiological and biochemical characteristics of THSD7A still remain. For example, although zebrafish *thsd7a* was prominently detected in the developing nervous system, the specific neural cell type that

expresses *thsd7a* transcript is not clear. The biological function of Thsd7a in neurogenesis is obscure, too. On the other hand, the abundant expression of THSD7A in the human placenta also indicates its distinct role in mammals. Given its expression in placental vasculature, it is interesting to study the function of THSD7A in controlling vascular growth in the placenta-related disease, such as preeclampsia symptoms. Also, it is unclear if there is an expression change of THSD7A in any other type of developmental and/ or disease angiogenesis.

Table 1. Phenotype frequencies of ISV defects in embryos at 30-31 hpf.

Injection (ng)	Normal ISVs (%)	Aberrant ISVs (%)	Total Live embryos (experiment repeats)
MO1			
0.5	60.63 ± 2.88	39.37 ± 2.88	162 (3)
1	49.61 ± 1.95	50.39 ± 1.95	382 (6)
2	31.97 ± 3.25	68.03 ± 3.25	135 (3)
MO2			
4.5	77.59 ± 5.39	22.41 ± 5.39	129 (3)
9	50.70 ± 5.42	49.30 ± 5.42	500 (7)
18	39.55 ± 4.27	60.45 ± 4.27	169 (3)
msMO1			
1	90.05 ± 4.37	9.95 ± 4.37	284 (4)
2	66.44 ± 3.25	33.56 ± 3.25	171 (3)
msMO2			
9	94.74 ± 1.32	5.26 ± 1.32	283 (4)
18	83.09 ± 6.42	16.91 ± 6.42	173 (3)
MO1/ *thsd7a* mRNA			
1 / 0.8	65.17 ± 3.20	34.83 ± 3.20	246 (4)
MO2/ *thsd7a* mRNA			
9 / 0.8	75.49 ± 2.30	24.51 ± 2.30	159 (3)

Frequency was calculated as the number of embryos with the indicated phenotype divided by the number of live embryos in each experiment. Mean ± s.e.m. was estimated from experimental replicates.

Table 2. Phenotype frequencies of ISV defects in embryos at 50 hpf.

Injection (ng)	Normal ISVs (%)	Aberrant ISVs (%)	Total Live embryos (experiment repeats)
MO1 (1)	43.81 ± 6.21	56.19 ± 6.21	119 (4)
MO2 (18)	45.16 ± 6.52	54.84 ± 6.52	190 (3)
msMO1 (1)	81.36 ± 5.04	18.64 ± 5.04	142 (4)
msMO2 (18)	85.15 ± 1.90	14.85 ± 1.90	227 (3)
MO1/ *thsd7a* mRNA (1/0.8)	68.13 ± 4.78	31.87 ± 4.78	153 (3)
MO2/ *thsd7a* mRNA (18/0.8)	65.31 ± 6.90	34.69 ± 6.90	143 (3)

Frequency was calculated as the number of embryos with the indicated phenotype divided by the number of live embryos in each experiment. Mean ± s.e.m. was estimated from experimental replicates.

TSING HUA UNIVERSITY

Table 3. Phenotype frequencies of circulation defects in embryos at 50 hpf.

Injection (ng)	Normal (%)	Absent axial circulation (%)	Absent ISV circulation (%)	Total Live embryos (experiment repeats)
MO1 (1)	80.36 ± 5.51	15.48 ± 5.39	4.15 ± 0.51	119 (4)
MO2 (18)	70.41 ± 12.89	11.67 ± 6.44	17.91 ± 8.77	96 (3)
msMO1 (1)	83.93 ± 4.23	8.13 ± 2.71	7.95 ± 6.17	142 (4)
msMO2 (18)	92.45 ± 5.28	7.55 ± 5.28	0 ± 0	115 (3)

Frequency was calculated as the number of embryos with the indicated phenotype divided by the number of live embryos in each experiment. Mean ± s.e.m. was estimated from experimental replicates.

TSING HUA UNIVERSITY

Fig. 1. Domain analysis of THSD7A amino acid sequence.

The full-length cDNA sequence of THSD7A predicts a polypeptide of 1,657 amino acids. Motifs identified by profile analysis are labeled as follows. Red: signal peptide sequence. Orange: RGD binding site. Blue: putative transmembrane domain. Green: CD36-binding motif. Purple: WSXW motif. Underlined: TSR.

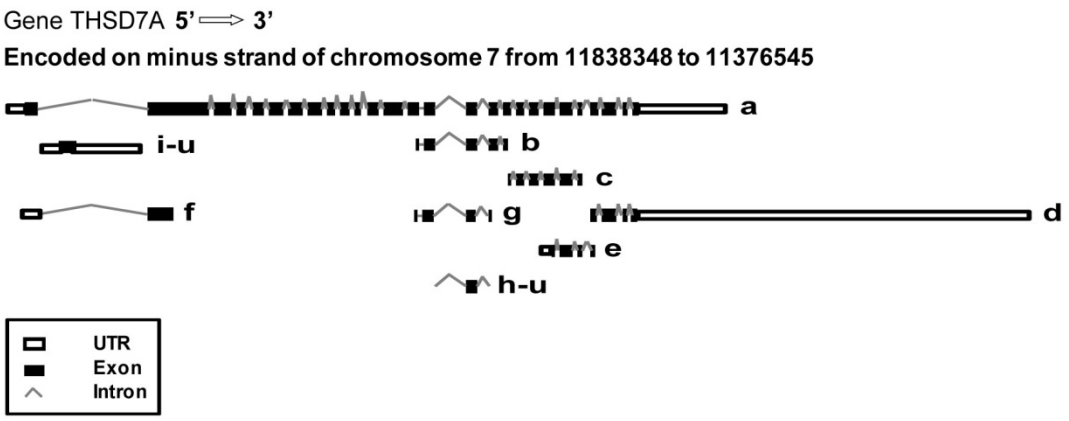

Fig. 2. *THSD7A* transcription is predicted to produce 9 different mRNA variants.

Gene annotation was retrieved from NCBI AceView*. *THSD7A* is encoded on the minus strand of chromosome 7 from 11838348 to 11376545. Virtual prediction of *THSD7A* transcription produces nine different mRNAs, including seven alternatively spliced variants (a-g) and two unspliced forms (h-u and i-u).

*http://www.ncbi.nlm.nih.gov/IEB/Research/Acembly/av.cgi?exdb=AceView&db=36a&term=THSD7A&submit=Go

HSING HUA UNIVERSITY

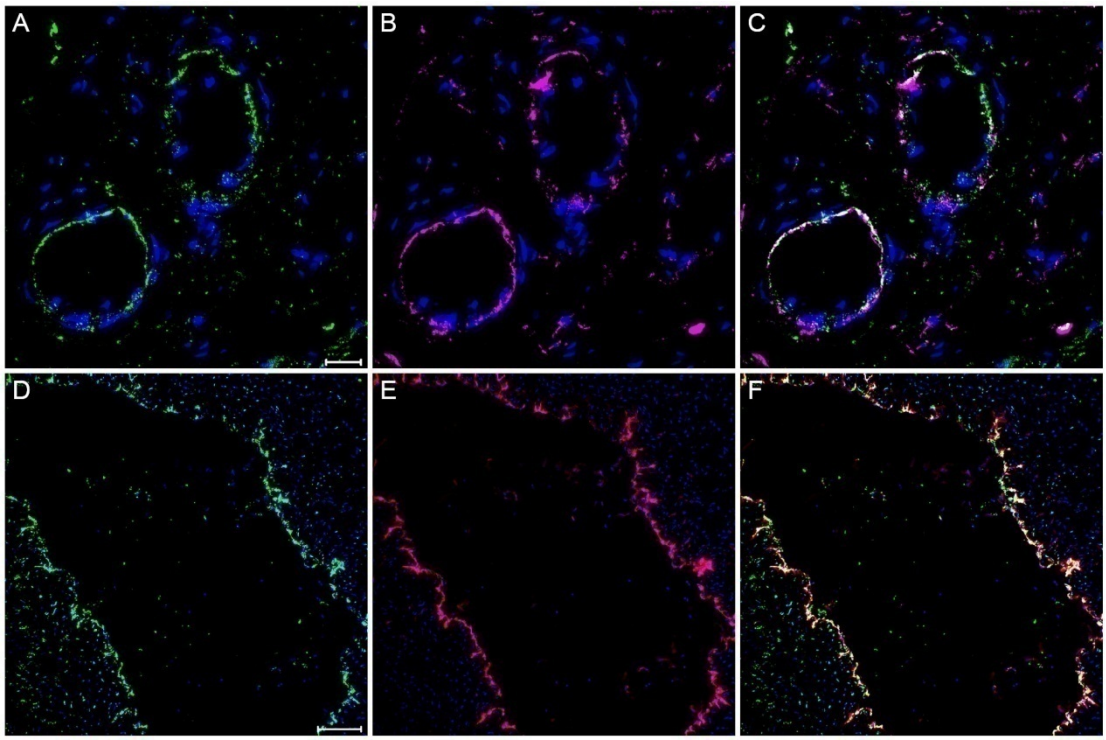

Fig. 3. THSD7A protein is expressed in placenta endothelial cells.

Protein expression of THSD7A in placental endothelium and umbilical vein endothelial cells was examined by fluorescent immunohistochemistry. (A) THSD7A (green) expressed in placenta (B) PECAM-1 (red) was used to reveal the location of endothelial cells. (C) Co-localization of THSD7A and PECAM-1 appears as yellow in the placental endothelium. (D) THSD7A was detected in the umbilical vein. (E) PECAM-1 expression in vein endothelial cells. (F) Co-localization of THSD7A and PECAM-1 in vein endothelial cells. Scale bars represent 20 μm (A) and 100 μm (D).

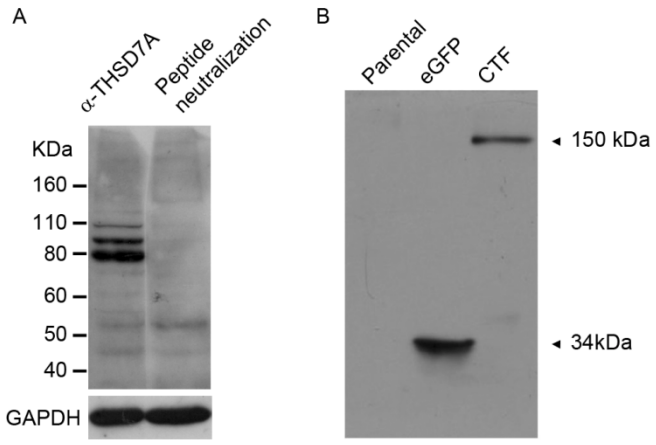

Fig. 4. Western blot analysis of THSD7A expression in HUVECs.

(A) Three major protein variants of 100, 88, and 78 KDa were detected. Lane 1, Western blot of a protein extract from HUVECs using α-THSD7A antibody; lane 2, Western blot of HUVEC extract using α-THSD7A antibody (1:500 dilution) together with peptide epitope neutralization (1:250 dilution). GAPDH was blotted as a loading control. (B) Expression of eGFP-fused THSD7A-CTF in HUVECs was examined. Cell lysates were extracted from untreated HUVECs (Parental) or cells transfected with pEGFPC3 empty vector (eGFP) or THSD7A-CTF-pEGFPC3 vector (CTF). The lysates were then subjected to electrophoresis followed by western blotting with goat anti-GFP antibody (NOVUS). THSD7A-CTF was clearly detected at around 150 kDa. eGFP expression as a positive control was detected at 34 kDa.

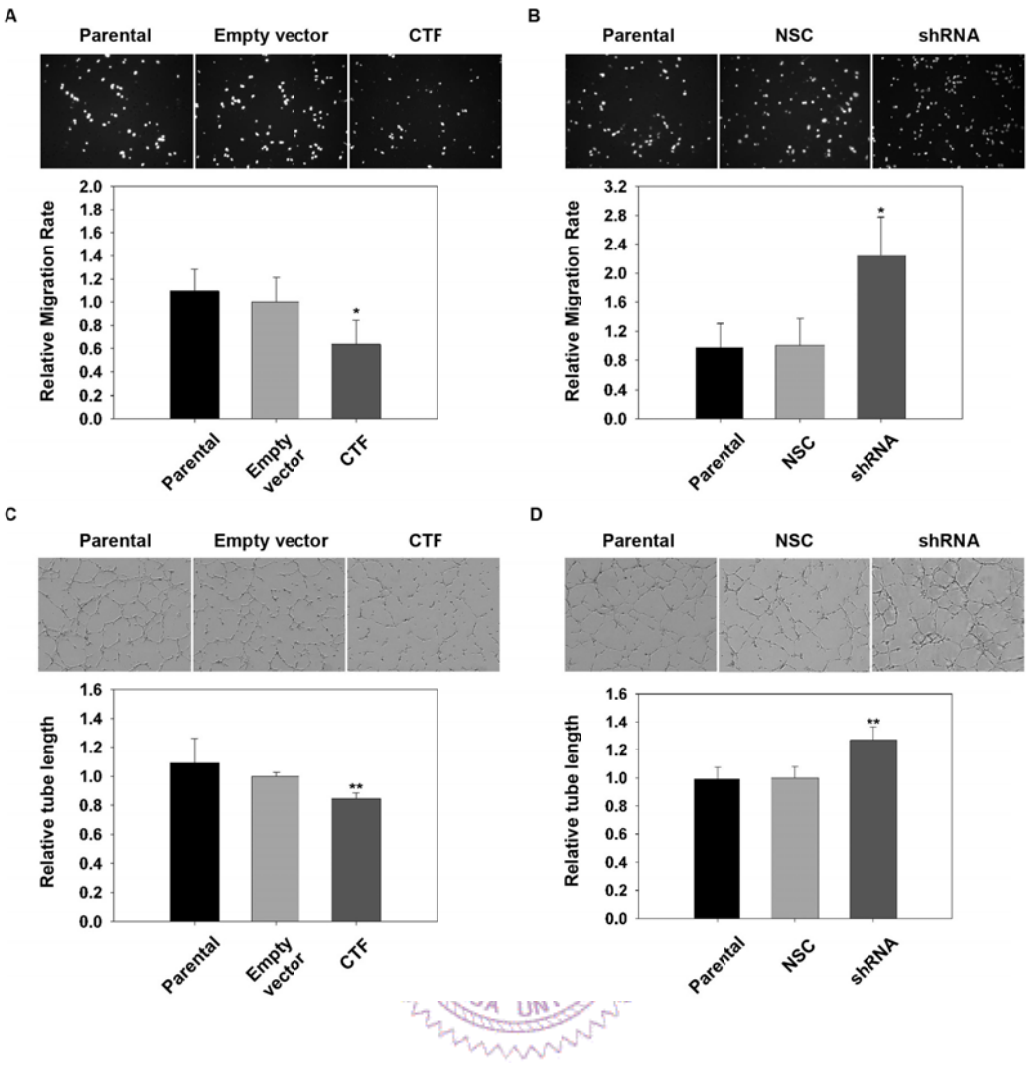

Fig. 5. THSD7A inhibits HUVEC migration and tube formation.

The contribution of endogenous THSD7A to HUVEC behavior was examined by the transwell migration assay and matrigel-induced tube formation assay. (A) Overexpression of THSD7A-CTF in HUVECs reduced the cell migration rate by 36.4% when compared to the parental untreated cells or cells transfected with empty vector. The relative migration rate in each treatment was normalized to empty-vector control and presented as the mean ±s.e.m. (*P<0.05 vs. empty vector) (B) HUVECs infected with THSD7A-specific shRNA lentivirus showed a two-fold increase of cell migration rate compared to the parental untreated cells or non-silencing controls (NSC). (*P<0.05 vs. NSC) (C) Amplification of THSD7A-CTF in HUVECs reduced tube formation activity by 15.5% in the tube formation assay. Data are presented as means of relative tube length of each field ±s.e.m. (**P<0.01 vs. empty vector) (D) Silencing of THSD7A in HUVECs enhanced tube formation by 27.0%. (**P<0.01 vs. NSC). Each experiment was performed in triplicate and repeated at least three times.

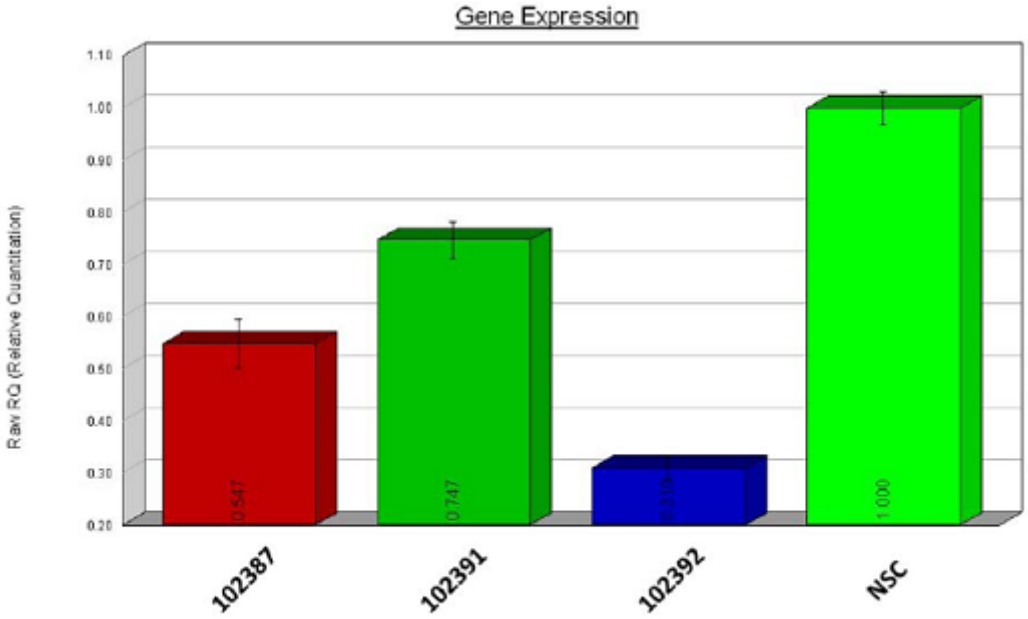

Fig. 6. *THSD7A* expression is down-regulated in HUVECs by shRNA interference.

The efficacy of three shRNA interference probes was evaluated by RT-qPCR. RNA extracted from HUVECs transformed with shRNA probe 102387, 102391, 102392, or a non-silencing control (NSC) were reverse-transcribed to cDNA for amplification. The expression level of THSD7A was normalized to beta-actin. Data were analyzed by Sequence Detection Software (Applied Biosystems) and presented as the RQ mean value ±s.e.m.

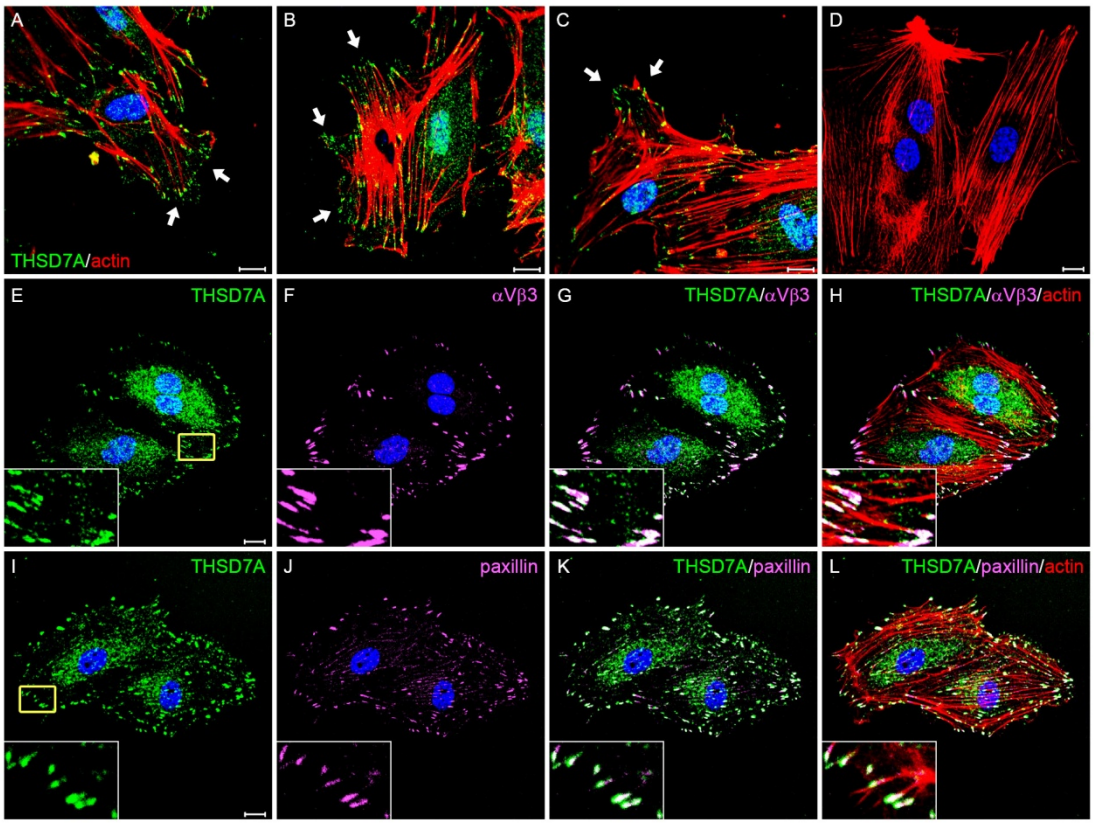

Fig. 7 THSD7A is co-localized with $\alpha_V\beta_3$ integrin and paxillin at the extremities of the cytoskeleton in HUVECs.

The distribution of THSD7A in HUVECs was examined by immunostaining. Nuclei were stained using DAPI (blue). The actin cytoskeleton was stained using phalloidin (red). Images were captured using a confocal microscope (LSM510 Meta, Zeiss). Inset images are enlarged views of the yellow boxed region. (A-C) Expression of THSD7A (green) was detected at the extremities of the actin cytoskeleton in the leading edge of migrating HUVECs (indicated by white arrows). (D) Peptide epitope neutralization control for antibody specificity. (E, I) Subcellular localization of THSD7A in HUVECs was detected at focal adhesions and the perinuclear area. (F, J) Expression pattern of $\alpha_V\beta_3$ integrin and paxillin (pink), respectively. (G, K) Co-localization of THSD7A with $\alpha_V\beta_3$ integrin and paxillin staining appears as a white color. (H, L) Full-color merged image reveals the distribution pattern of THSD7A with $\alpha_V\beta_3$ integrin and paxillin in association with the cytoskeleton. Scale bar represents 10 μm.

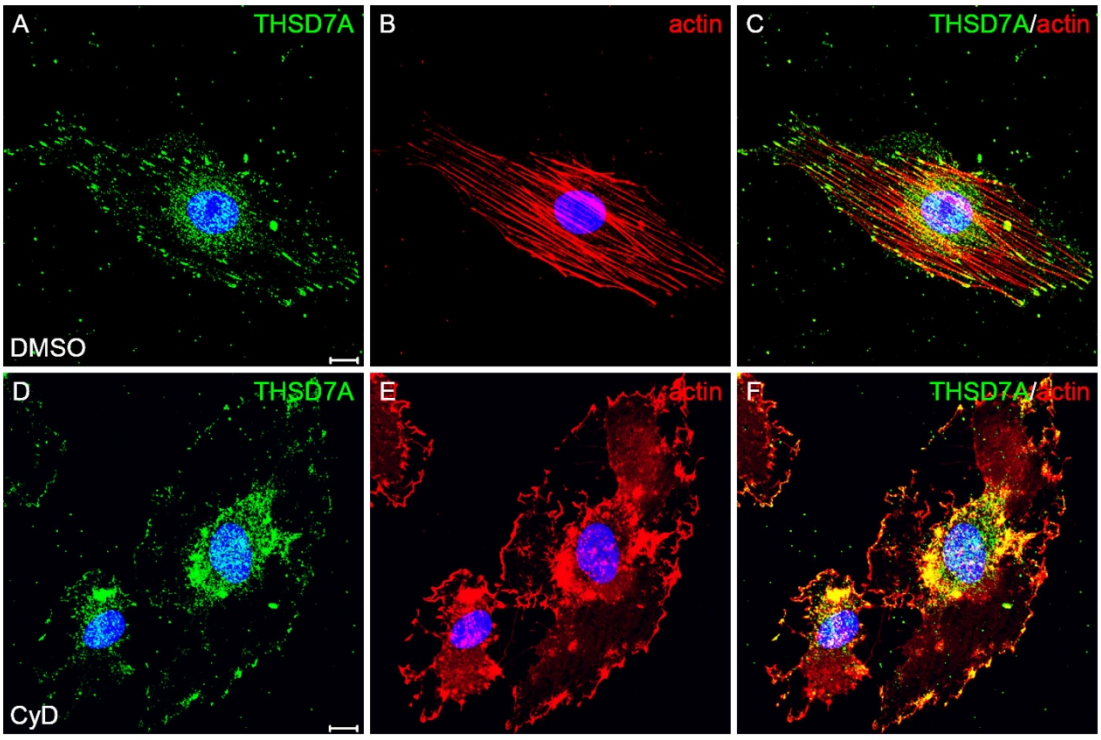

Fig. 8. THSD7A disperses from focal adhesions upon inhibition of actin polymerization.

Subcellular localization of THSD7A was examined after disassembly of the actin cytoskeleton. (A-C) THSD7A localized at focal adhesions in HUVECs treated with DMSO. (D-F) HUVECs were treated with 10 μM CyD for 15 minutes. THSD7A dispersed from focal adhesions and into actin aggregates. Scale bar represents 10 μm.

A

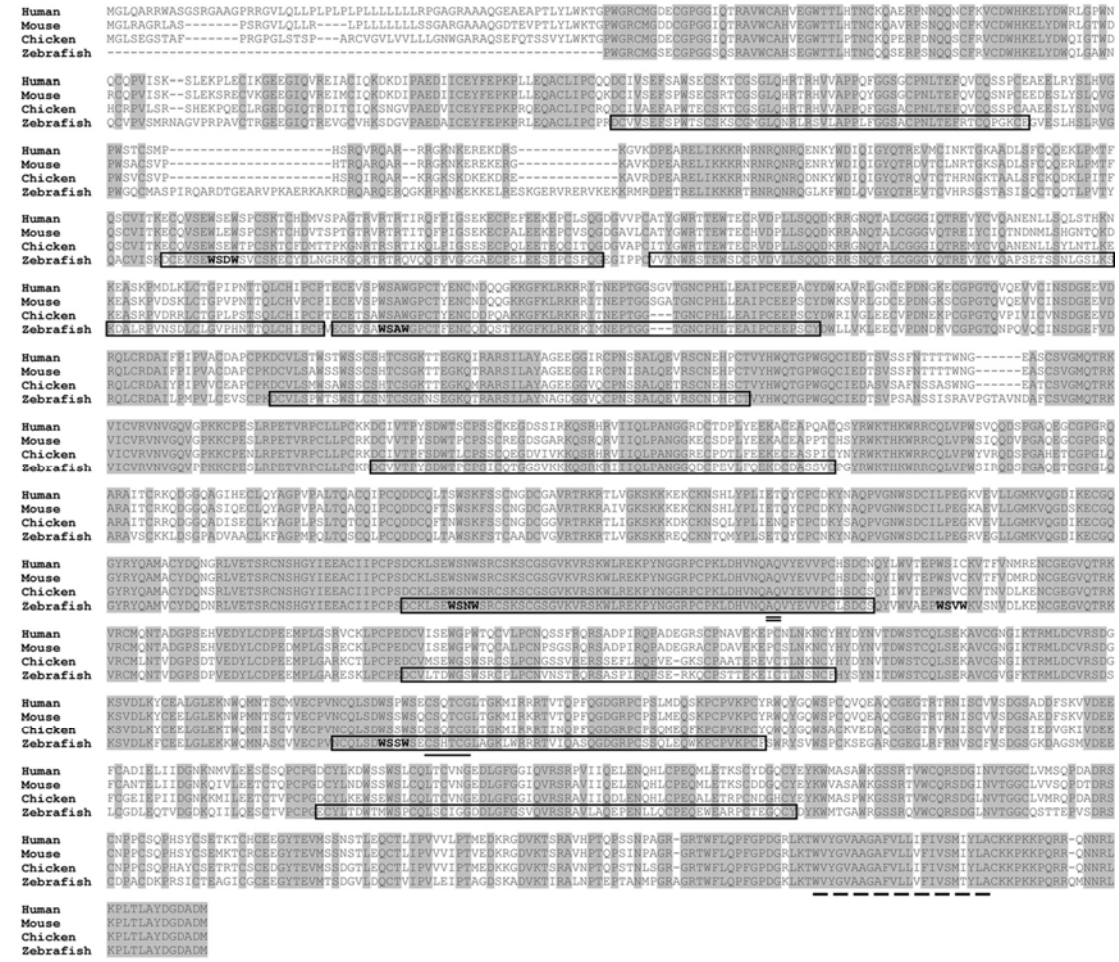

B

	Zebrafish	Chicken	Mouse	Human
Zebrafish	-	69	68	69
Chicken		-	80	83
Mouse			-	90
Human				-

C

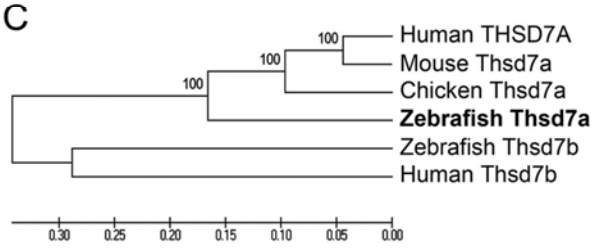

Fig. 9. Thsd7a is conserved among vertebrates.

(A) Comparison of the deduced amino acid sequence of zebrafish Thsd7a to orthologs from other species. Identical amino acids are shaded. The boxed sequences in Thsd7a indicate the TSRs. The putative TGF-β binding sites are in bold. The CD36-binding site is underlined. Dashed-underline indicates the putative transmembrane domain. Double-underline indicates the two-amino acid insertion. (B) Percent amino acid identity among Thsd7a orthologs in different species. (C) Phylogenetic analysis of Thsd7a orthologs in different species by the neighbor-joining method. Thsd7b orthologs are shown as references. Identical in-group topologies were also obtained from the maximum-parsimony and maximum-likelihood methods. Numbers at the nodes indicate bootstrap values with 1000 replicates (expressed as percentage). The bar indicates evolutionary distance. (GenBank accession numbers: HQ267705, NP056019.1, XP287555.6, XP418686.2)

TSING HUA UNIVERSITY

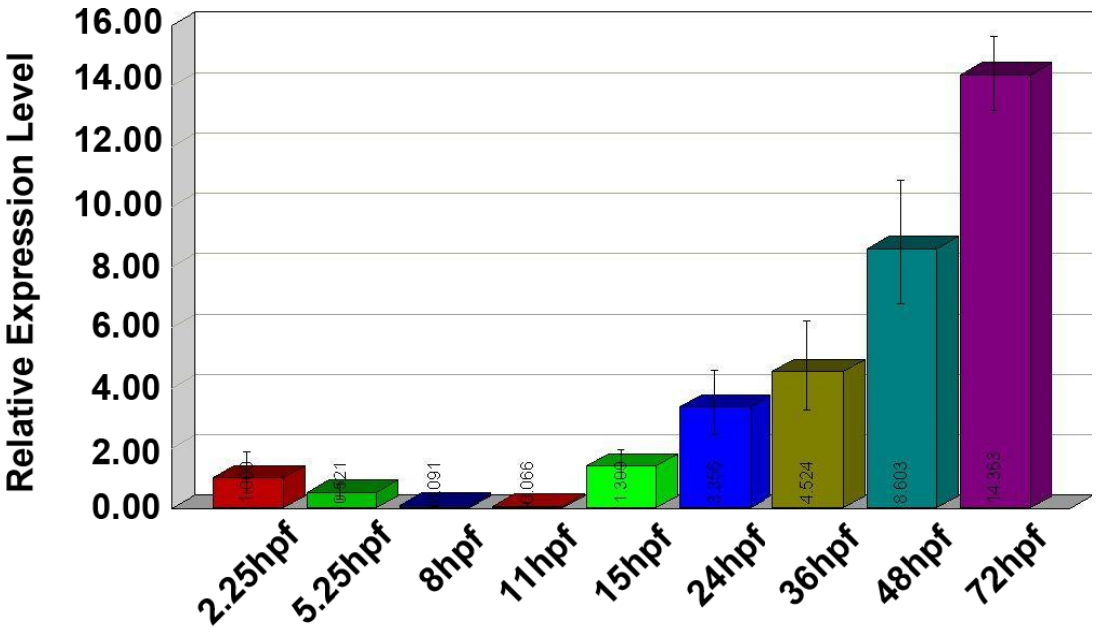

Fig. 10. *thsd7a* expression levels increase during embryogenesis.

RT-qPCR was performed on zebrafish embryos at different developmental stages. The *thsd7a* expression level was first normalized by *beta-actin* expression and then by the level at stage 2.25 hpf, and was plotted as mean ± s.e.m. A small amount of *thsd7a* transcript was detected at 2.25 hpf. Zygotic *thsd7a* was up-regulated at 15 hpf and persistently increased during the examined developmental period.

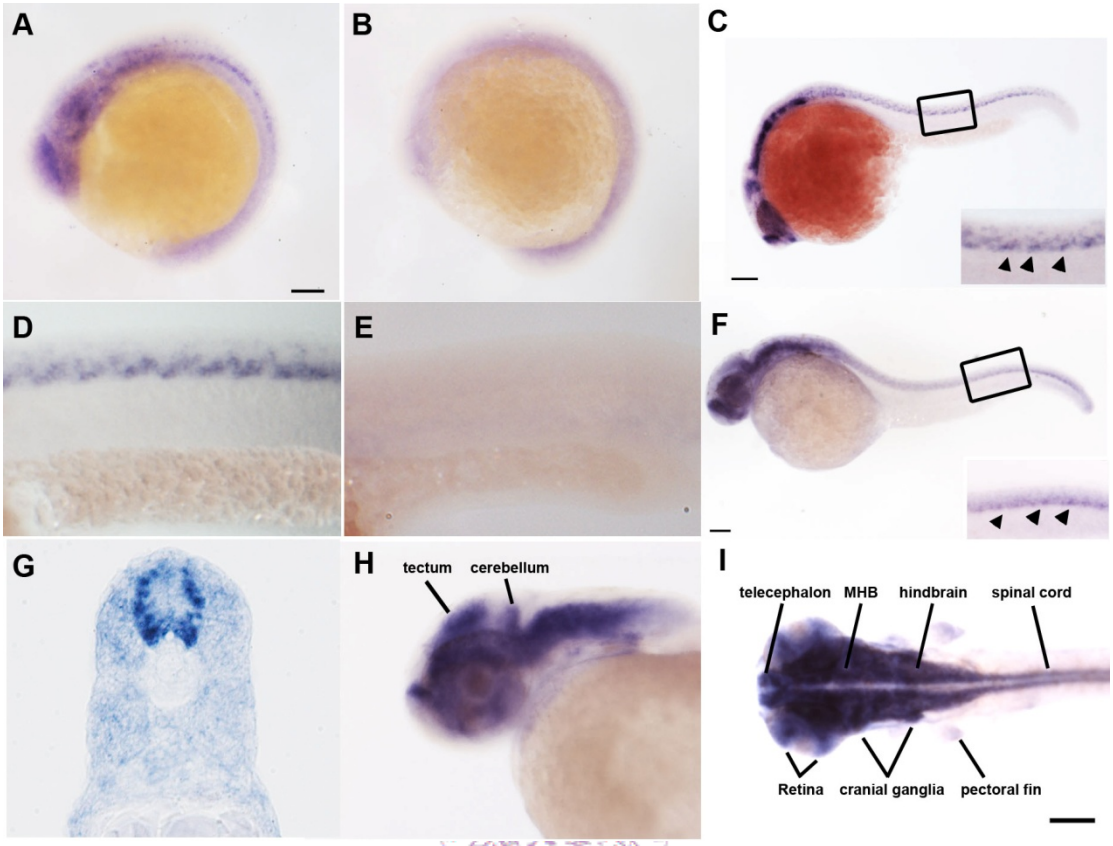

Fig. 11. *thsd7a* transcripts were detected in the zebrafish developing nervous system.

Representative embryos show the spatiotemporal expression pattern of *thsd7a* transcripts by *in situ* hybridization. Anterior is to the left. (A) *thsd7a* expression was first detected at 15 hpf. (B) An embryo stained with control probe at 15 hpf. (C) 22 hpf. The inset image is an enlarged view of the boxed region. The unique *thsd7a* expression pattern along the ventral edge of neural tube is indicated by arrowheads. (D) Higher-magnification imaging of ISH showed *thsd7a* expression in the neural tube of an embryo at 22 hpf. (E) An embryo stained with control probe at 22 hpf. (F) 32hpf. Expression of *thsd7a* along the ventral edge of neural tube is indicated by arrowheads in the inset image enlarged from boxed region. (G) Cross-section through the trunk region at 32 hpf. (H, I) At 48 hpf, *thsd7a* is expressed in the midbrain, hindbrain, midbrain-hindbrain boundary, cerebellum, telencephalon, tectum, retina, cranial ganglia, spinal cord, and pectoral fin. (I) Dorsal view. Scale bars represent 20 μm (A), 50 μm (C) and 100μm (F, I).

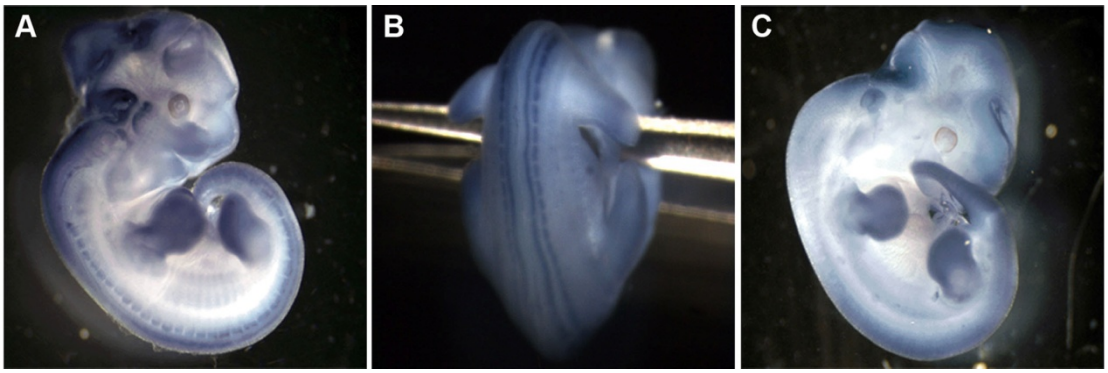

Fig. 12. The mouse *Thsd7a* ortholog is expressed in the central nervous system at E12.5.

Representative embryos show the expression pattern of the mouse *Thsd7a* ortholog by *in situ* hybridization. (A-B) *Thsd7a* mouse ortholog is selectively expressed in the midbrain, hindbrain, neural tube, and dorsal root ganglia in the E12.5 embryo. (A) Lateral view. (B) Dorsal view. (C) Background control (in collaboration with Dr. Jana Hoffman and Dr. Calvin Kuo).

TSING HUA UNIVERSITY

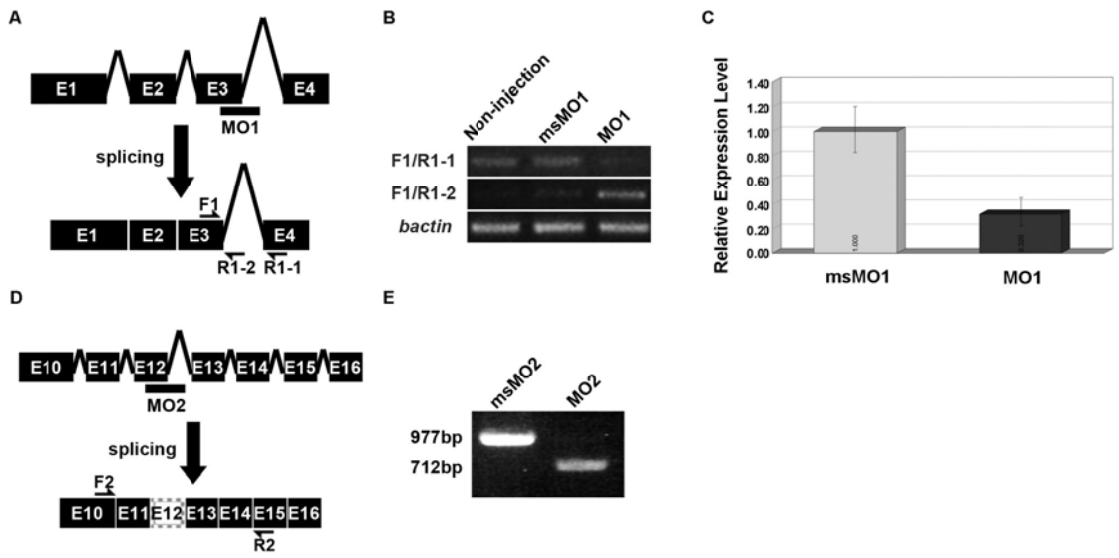

Fig. 13. Morpholino knockdown of Thsd7a in zebrafish embryos.

(A) The genomic structure of Thsd7a showing the effect of MO1 injection on mRNA splicing. Relative positions of primers used for RT-PCR are shown. (B) MO1 injection disrupted the accurate mRNA splicing. RT-PCR products using the F1/R1-1 primer pair reveal the level of accurate mRNA splicing. Products using the F1/R1-2 primer pair show the level of mRNA containing the retained intron. *Beta-actin* (*bactin*) was amplified as an internal control. 2ng of MO1/ msMO1 were injected. (C) RTq-PCR was performed to quantify the efficacy of Thsd7a MO1 knockdown in zebrafish embryos. Relative expression levels of *Thsd7a* transcript in msMO1- and MO1-injected embryos were plotted as mean ± s.e.m. 2ng of MO1/ msMO1 were injected. (D) MO2 targets the splice junction of the twelfth exon. Relative positions of primers used for RT-PCR are shown. (E) Amplification product using cDNA derived from msMO2 embryos showed the expected 977 base pair fragment. MO2 injection resulted in a shorter PCR product of 712 base pairs. 18ng of MO2/ msMO2 were injected.

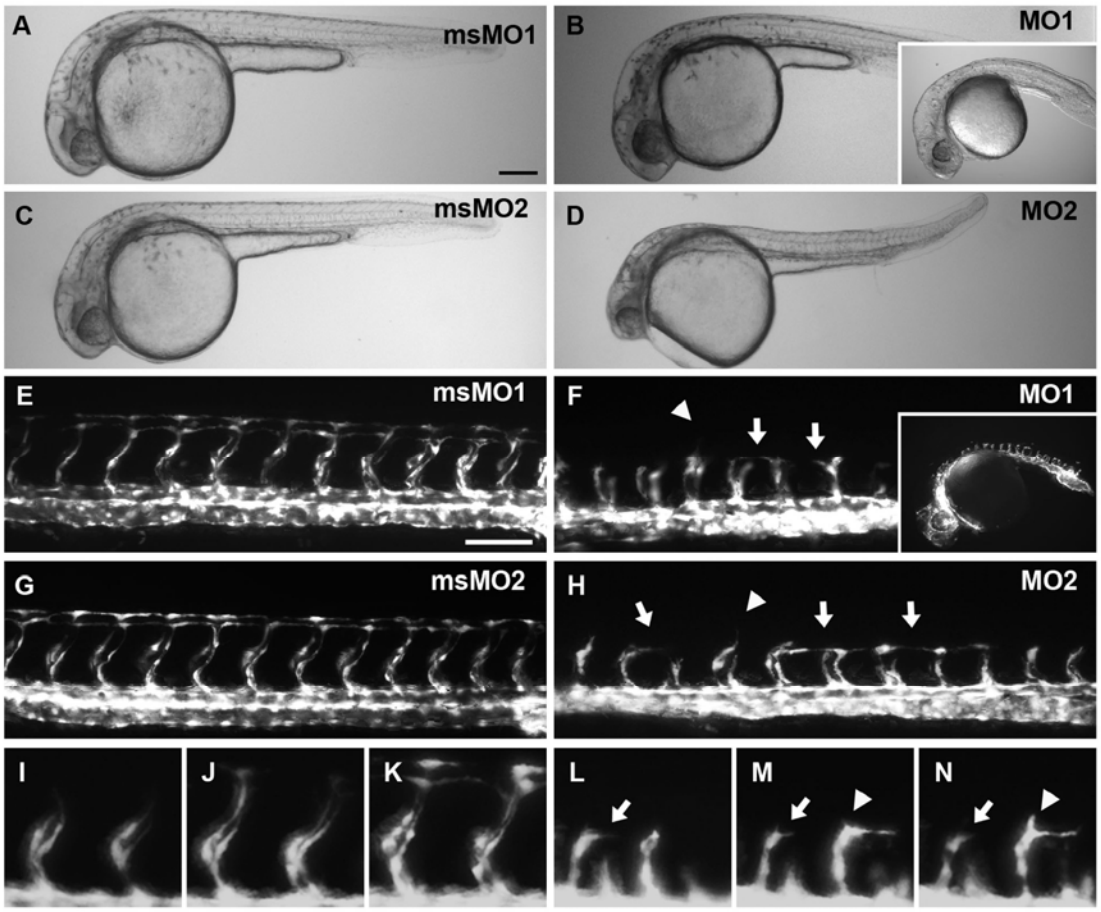

Fig. 14. Knockdown of Thsd7a impairs ISV angiogenesis.

Representative images showed the effect of Thsd7a knockdown on ISV angiogenesis. Anterior is to the left. Embryos were examined at 29-31 hpf, except where indicated. (A, C, E, G) Embryos injected with msMOs. (B, D, F, H) Embryos injected with 1ng of MO1 (B, F; the inset images in panels B and F show a representative embryo injected with 2 ng of MO1) and 9 ng of MO2 (D, H). (E, G) Complete ISV networks were formed in embryos injected with msMO1 (E) or msMO2 (G). (F, H) Aberrant ISV patterning was observed in embryos injected with MO1 (F) or MO2 (H). Lateral deviation is indicated by white arrows. ISVs that reached the roof of the neural tube are indicated by white arrowheads. (I-N) ISV patterning in embryos injected with 1ng of msMO1 (I-K) or 1 ng of MO1 (L-N) at 24 hpf (I, L), 30 hpf (J, M), and 36 hpf (K, N). White arrows in panels L and M indicate the EC that extended and retracted filopodia. Arrowheads in panels M and N indicate a lamellipodia-like structural extension. Scale bars represent 200 μm (A) and 100 μm (E).

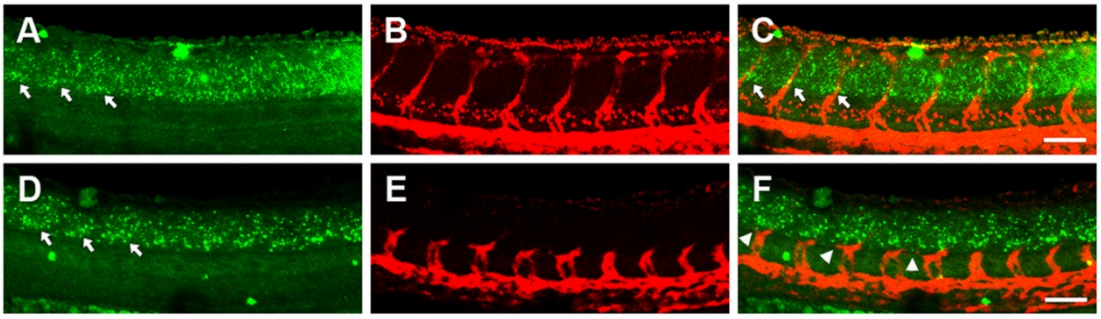

Fig. 15. Spatial relationship between *Thsd7a* expression and the ISV pattern.

Expression of *Thsd7a* transcript (green) was detected by fluorescent ISH, followed by immunostaining to reveal the ISV pattern (red). Anterior is to the left. Segmental *Thsd7a* expression is indicated by white arrows. Lateral deviation is indicated by white arrowheads. (A-C) Representative images showing the control embryo at 30 hpf. (D-F) Morphant at 30 hpf. Scale bars represent 50 μm.

TSING HUA UNIVERSITY

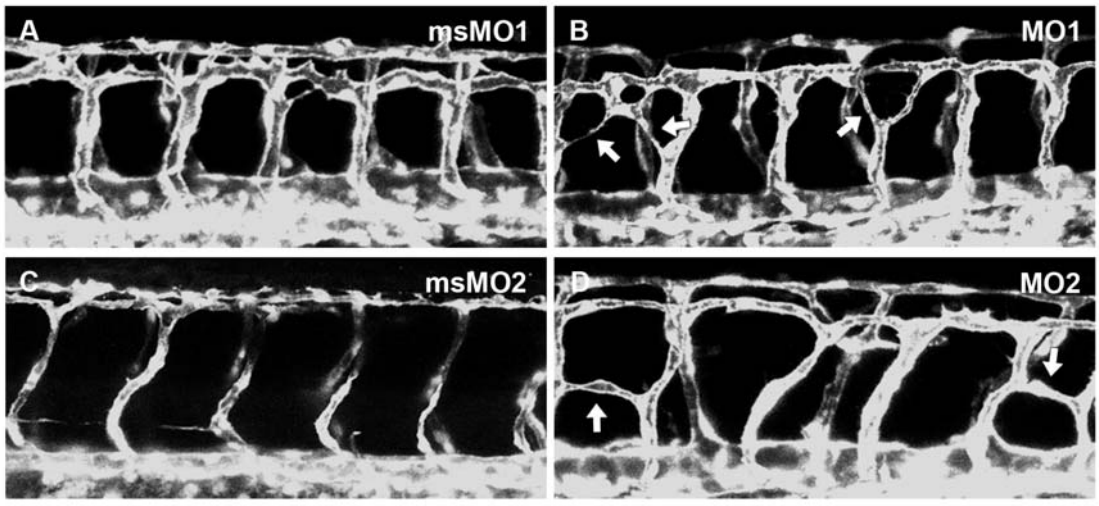

Fig. 16. Knockdown of Thsd7a impairs ISV patterning at 50hpf.

Representative images of ISV network in the control siblings (A, C) and the morphants (B, D) at 50hpf. Anterior is to the left. Abnormal ISV branches are indicated by white arrows.

TSING HUA UNIVERSITY

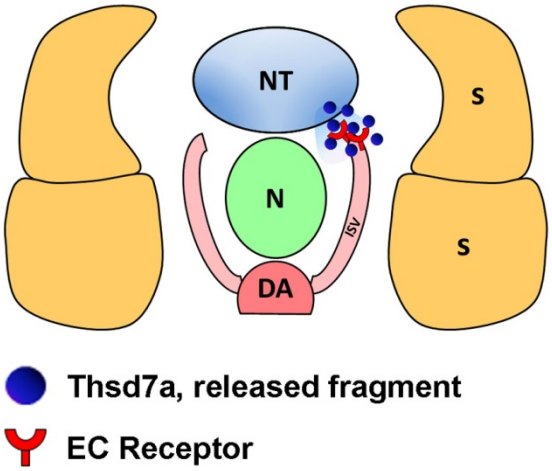

Fig. 17. The model for the role of Thsd7a in endothelial cell migration during ISV angiogenesis.

Fragments of Thsd7a may be released from neural cells, and form a concentration gradient that guide EC migration during ISV angiogenesis. Abbreviations: NT, neural tube; N, notochord; DA, dorsal aorta; ISV, intersegmental vessel; S, somite.

HUA UNIVERSITY

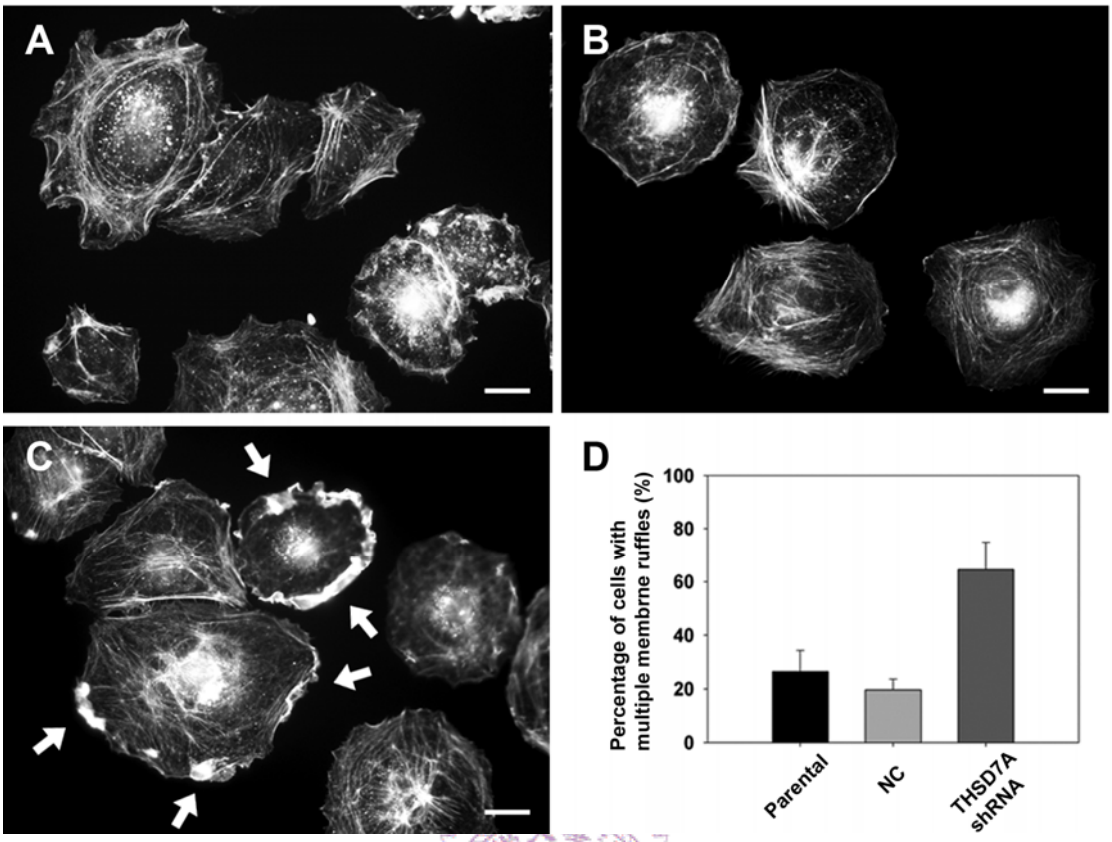

Fig. 18. Knockdown of THSD7A in HUVECs induces multiple membrane ruffles.

Representative images showing the structure of the actin cytoskeleton in HUVECs. (A) Untreated parental cells. (B) Cells treated with non-silencing control virus. (C) Cells treated with THSD7A shRNA. Membrane ruffling is indicated by white arrows. (D) Quantitative analysis showed a significant increase in multiple membrane ruffles in cells treated with *THSD7A* shRNA as compared to parental cells or non-silencing control cells (NC). Each experiment was performed in triplicate and repeated three times. (*P<0.01 vs. NC). Scale bars represent 20 μm.

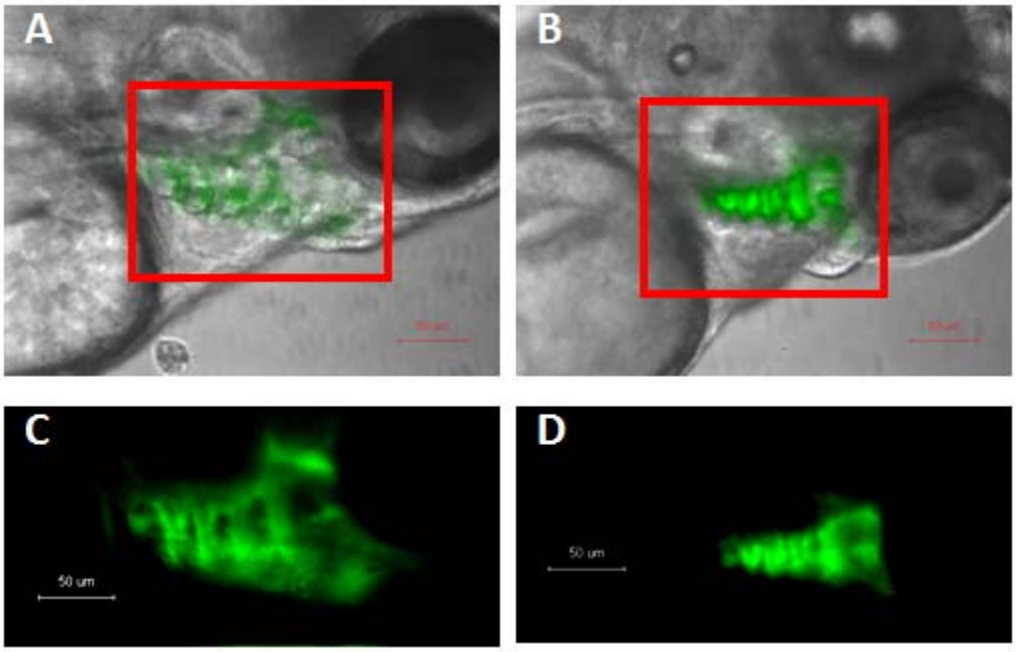

Fig. 19. Knockdown of Thsd7a causes developmental defects of aortic arches at 3 day post-fertilization.

Anterior is to the right. Lateral views of a control (A) and the Thsd7a morphant (B). (C) The boxed region in panel A showed the normal aortic arch structure. (D) The boxed region in panel B indicated stunted aortic arch development in the morphant.

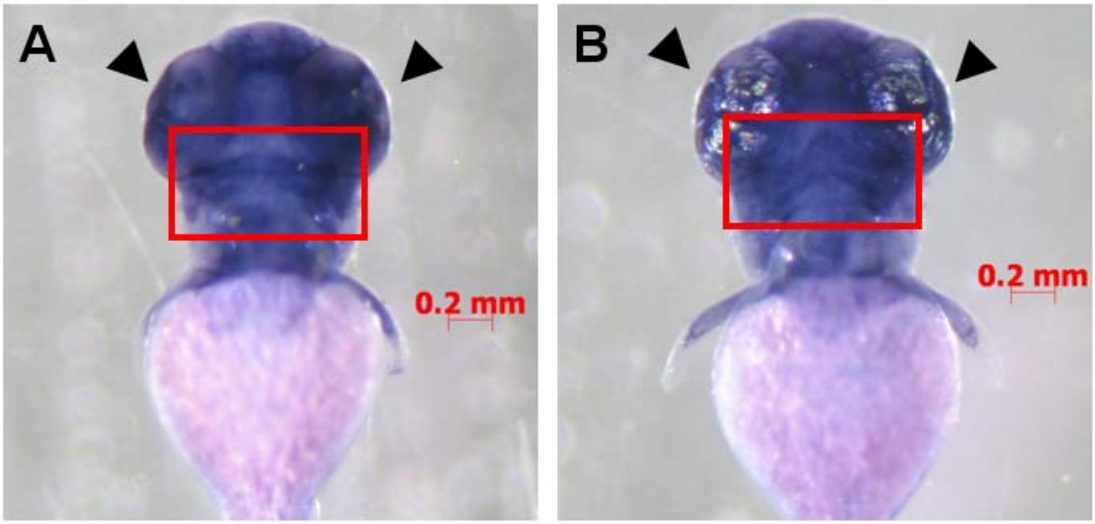

Fig. 20. Thsd7a knockdown disrupts vascular development.

Ventral views of the Thsd7a morphant (A) and the control (B). The boxed region showed a disconnection between aortic arch and dorsal aorta in the morphant (A), when compared to the normal vessel development in the control (B). Arrowheads indicated the vasculature in eyes.

TSING HUA UNIVERSITY

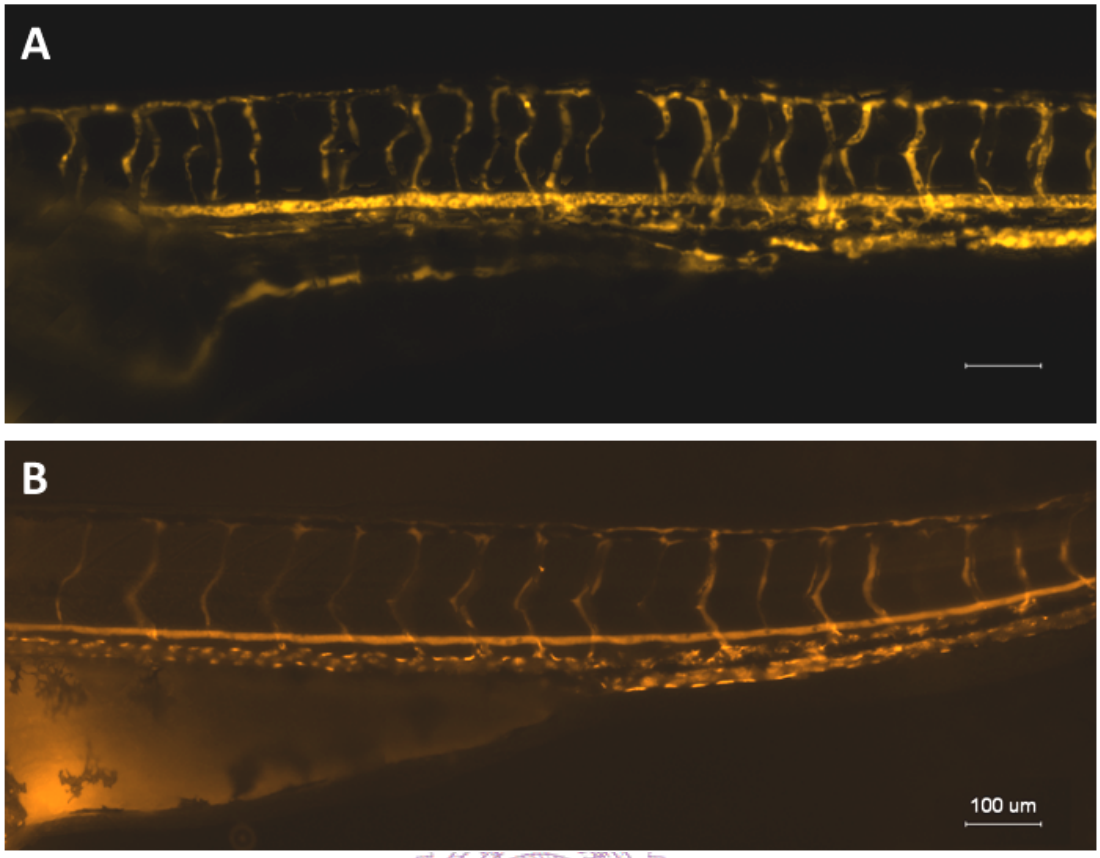

Fig. 21. Blood circulation follows the ISV structure.

Microangiography was performed to reveal the blood circulation in the ISVs in the morphant (A) and the control (B). Anterior is to the left.

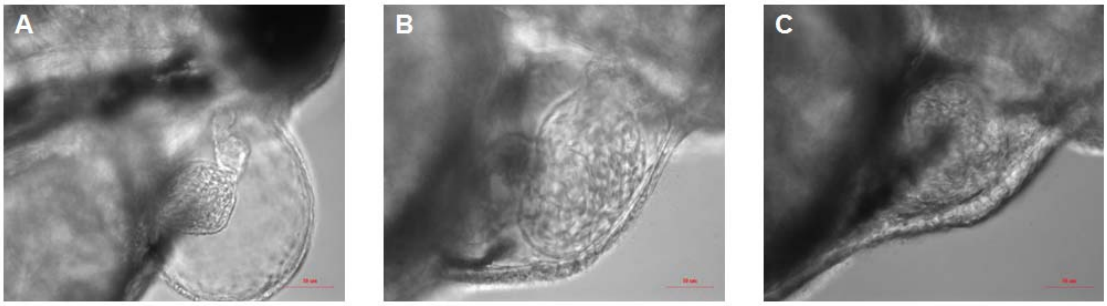

Fig. 22. Heart phenotypes in the morphant and the control.

Anterior is to the right. Injection of morpholino caused pericardial edema (A), and enlarged heart (B) at 3 dpf, when compared to the control (C).

TSING HUA UNIVERSITY

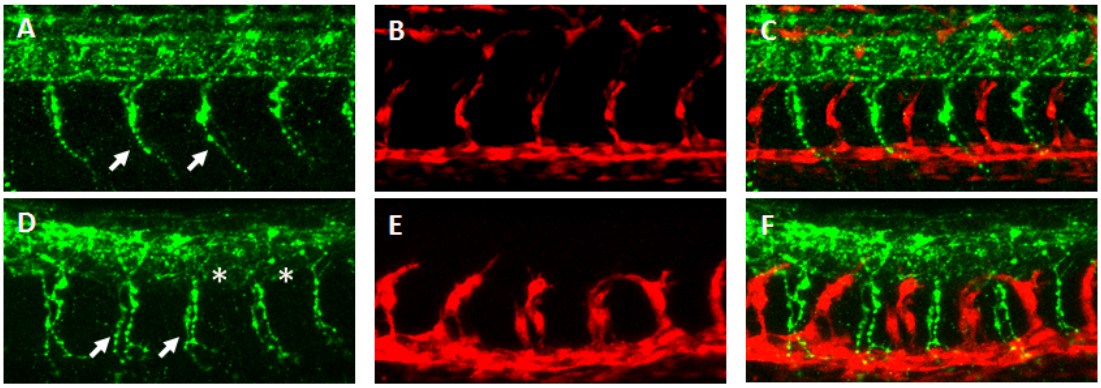

Fig. 23. Thsd7a is required for intraspinal motor axon development.

Representative images of motoneuron defects caused by Thsd7a down-regulation. (A-C) msMOs injection. (D-F) Morpholino knockdown of Thsd7a caused abnormal intraspinal motoneuron development. Axon projections of caudal motoneuron are indicated by while arrows (A, D). Truncated trajectories of middle primary motoneuron are indicated by white asterisks (D). Color code: Green, primary motoneuron; Red, intersegmental vascular endothelial cells.

TSING HUA UNIVERSITY

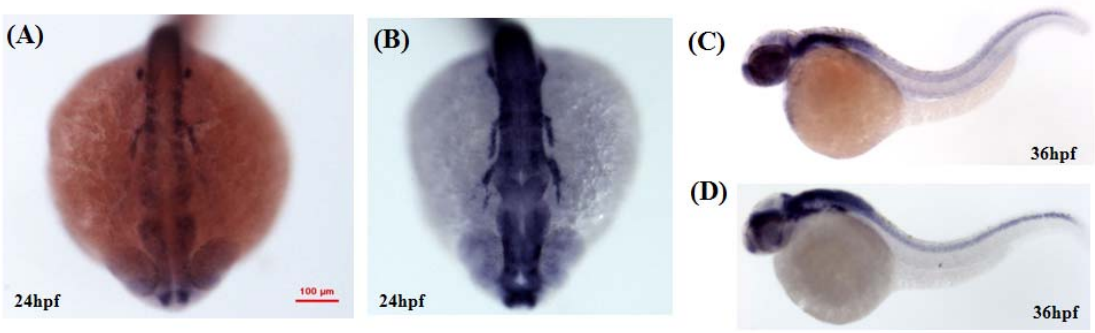

Fig. 24. *thsd7a* expression co-localizes with the neural stem cell pan marker, *nestin*.

The expression pattern of *thsd7a* (A, C) corresponds with *nestin* (B, D) at cranial ganglia, telecephalon, retina, MHB, and spinal cord at 24hpf and 36hpf.

TSING HUA UNIVERSITY

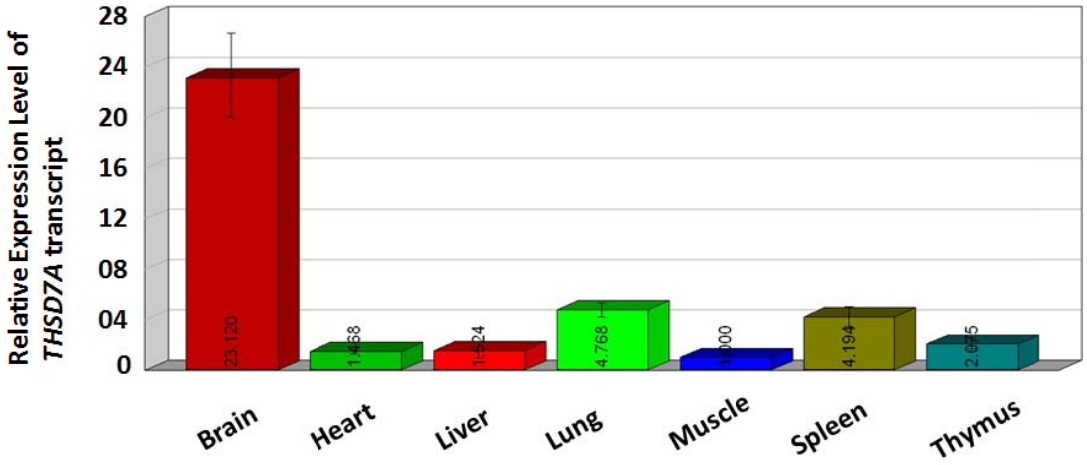

Fig. 25. *THSD7A* transcript was prominently expressed in the human fetal brain.

RT-qPCR was performed on cDNA libraries derived from different human fetal tissues. The *THSD7A* expression level was first normalized by *GAPDH* expression, and was plotted as mean ± s.e.m. Expression of *THSD7A* transcript was detected in a relative high level in the fetal brain.

TSING HUA UNIVERSITY

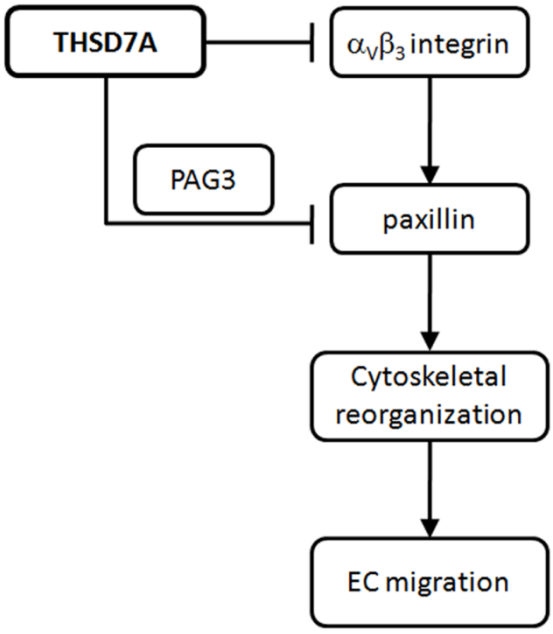

Fig. 26. Model for the role of THSD7A in endothelial cell migration.

THSD7A may block $\alpha_V\beta_3$ integrin-mediated signal transduction. THSD7A may cooperate with PAG3 to hinder paxillin recruitment to the focal complexes. These possible interactions result in cytoskeletal reorganization to mediate EC migration.

CHUNG HUA UNIVERSITY

References

1. Cleaver, O. & Melton, D.A. Endothelial signaling during development. *Nat Med* 9, 661-668 (2003).
2. Suchting, S., Bicknell, R. & Eichmann, A. Neuronal clues to vascular guidance. *Exp Cell Res* 312, 668-675 (2006).
3. Folkman, J. Angiogenesis: an organizing principle for drug discovery? *Nat Rev Drug Discov* 6, 273-286 (2007).
4. Carmeliet, P. Mechanisms of angiogenesis and arteriogenesis. *Nat Med* 6, 389-395 (2000).
5. Djonov, V., Schmid, M., Tschanz, S.A. & Burri, P.H. Intussusceptive angiogenesis: its role in embryonic vascular network formation. *Circ Res* 86, 286-292 (2000).
6. Kubis, N. & Levy, B.I. Understanding angiogenesis: a clue for understanding vascular malformations. *J Neuroradiol* 31, 365-368 (2004).
7. Djonov, V., Baum, O. & Burri, P.H. Vascular remodeling by intussusceptive angiogenesis. *Cell Tissue Res* 314, 107-117 (2003).
8. Dejana, E., Orsenigo, F. & Lampugnani, M.G. The role of adherens junctions and VE-cadherin in the control of vascular permeability. *J Cell Sci* 121, 2115-2122 (2008).
9. Fukumura, D. *et al.* Predominant role of endothelial nitric oxide synthase in vascular endothelial growth factor-induced angiogenesis and vascular permeability. *Proc Natl Acad Sci U S A* 98, 2604-2609 (2001).
10. Sawada, N., Salomone, S., Kim, H.H., Kwiatkowski, D.J. & Liao, J.K. Regulation of endothelial nitric oxide synthase and postnatal angiogenesis by Rac1. *Circ Res* 103, 360-368 (2008).
11. Pepper, M.S. Role of the matrix metalloproteinase and plasminogen activator-plasmin systems in angiogenesis. *Arterioscler Thromb Vasc Biol* 21, 1104-1117 (2001).
12. Egeblad, M. & Werb, Z. New functions for the matrix metalloproteinases in cancer progression. *Nat Rev Cancer* 2, 161-174 (2002).
13. Seandel, M., Noack-Kunnmann, K., Zhu, D., Aimes, R.T. & Quigley, J.P. Growth factor-induced angiogenesis in vivo requires specific cleavage of fibrillar type I collagen. *Blood* 97, 2323-2332 (2001).
14. Xu, J. *et al.* Proteolytic exposure of a cryptic site within collagen type IV is required for angiogenesis and tumor growth in vivo. *J Cell Biol* 154, 1069-1079 (2001).
15. Galvez, B.G., Matias-Roman, S., Albar, J.P., Sanchez-Madrid, F. & Arroyo, A.G.

Membrane type 1-matrix metalloproteinase is activated during migration of human endothelial cells and modulates endothelial motility and matrix remodeling. *J Biol Chem* 276, 37491-37500 (2001).

16. Davis, G.E., Koh, W. & Stratman, A.N. Mechanisms controlling human endothelial lumen formation and tube assembly in three-dimensional extracellular matrices. *Birth Defects Res C Embryo Today* 81, 270-285 (2007).
17. Koh, W., Mahan, R.D. & Davis, G.E. Cdc42- and Rac1-mediated endothelial lumen formation requires Pak2, Pak4 and Par3, and PKC-dependent signaling. *J Cell Sci* 121, 989-1001 (2008).
18. Hellstrom, M., Kalen, M., Lindahl, P., Abramsson, A. & Betsholtz, C. Role of PDGF-B and PDGFR-beta in recruitment of vascular smooth muscle cells and pericytes during embryonic blood vessel formation in the mouse. *Development* 126, 3047-3055 (1999).
19. Fukuhara, S. *et al.* Angiopoietin-1/Tie2 receptor signaling in vascular quiescence and angiogenesis. *Histol Histopathol* 25, 387-396 (2010).
20. Makanya, A.N. *et al.* Microvascular endowment in the developing chicken embryo lung. *Am J Physiol Lung Cell Mol Physiol* 292, L1136-1146 (2007).
21. Makanya, A.N., Stauffer, D., Ribatti, D., Burri, P.H. & Djonov, V. Microvascular growth, development, and remodeling in the embryonic avian kidney: the interplay between sprouting and intussusceptive angiogenic mechanisms. *Microsc Res Tech* 66, 275-288 (2005).
22. Suri, C. *et al.* Requisite role of angiopoietin-1, a ligand for the TIE2 receptor, during embryonic angiogenesis. *Cell* 87, 1171-1180 (1996).
23. Thurston, G. *et al.* Leakage-resistant blood vessels in mice transgenically overexpressing angiopoietin-1. *Science* 286, 2511-2514 (1999).
24. Oh, S.J., Kurz, H., Christ, B. & Wilting, J. Platelet-derived growth factor-B induces transformation of fibrocytes into spindle-shaped myofibroblasts in vivo. *Histochem Cell Biol* 109, 349-357 (1998).
25. Burri, P.H. & Djonov, V. Intussusceptive angiogenesis--the alternative to capillary sprouting. *Mol Aspects Med* 23, S1-27 (2002).
26. Kawakami, K. Tol2: a versatile gene transfer vector in vertebrates. *Genome Biol* 8 Suppl 1, S7 (2007).
27. Wienholds, E. & Plasterk, R.H. Target-selected gene inactivation in zebrafish. *Methods Cell Biol* 77, 69-90 (2004).
28. Meng, X., Noyes, M.B., Zhu, L.J., Lawson, N.D. & Wolfe, S.A. Targeted gene inactivation in zebrafish using engineered zinc-finger nucleases. *Nat Biotechnol* 26, 695-701 (2008).
29. Doyon, Y. *et al.* Heritable targeted gene disruption in zebrafish using

designed zinc-finger nucleases. *Nat Biotechnol* 26, 702-708 (2008).

30. Childs, S., Chen, J.N., Garrity, D.M. & Fishman, M.C. Patterning of angiogenesis in the zebrafish embryo. *Development* 129, 973-982 (2002).
31. Isogai, S., Lawson, N.D., Torrealday, S., Horiguchi, M. & Weinstein, B.M. Angiogenic network formation in the developing vertebrate trunk. *Development* 130, 5281-5290 (2003).
32. Eichmann, A., Makinen, T. & Alitalo, K. Neural guidance molecules regulate vascular remodeling and vessel navigation. *Genes Dev* 19, 1013-1021 (2005).
33. Baldessari, D. & Mione, M. How to create the vascular tree? (Latest) help from the zebrafish. *Pharmacol Ther* 118, 206-230 (2008).
34. Carmeliet, P. Blood vessels and nerves: common signals, pathways and diseases. *Nat Rev Genet* 4, 710-720 (2003).
35. Torres-Vazquez, J. *et al.* Semaphorin-plexin signaling guides patterning of the developing vasculature. *Dev Cell* 7, 117-123 (2004).
36. Lu, X. *et al.* The netrin receptor UNC5B mediates guidance events controlling morphogenesis of the vascular system. *Nature* 432, 179-186 (2004).
37. Weinstein, B.M. Vessels and nerves: marching to the same tune. *Cell* 120, 299-302 (2005).
38. Wang, C.H. *et al.* Thrombospondin type I domain containing 7A (THSD7A) mediates endothelial cell migration and tube formation. *J Cell Physiol* 222, 685-694 (2010).
39. Jaffe, E.A., Nachman, R.L., Becker, C.G. & Minick, C.R. Culture of human endothelial cells derived from umbilical veins. Identification by morphologic and immunologic criteria. *J Clin Invest* 52, 2745-2756 (1973).
40. Tamura, K., Dudley, J., Nei, M. & Kumar, S. MEGA4: Molecular Evolutionary Genetics Analysis (MEGA) software version 4.0. *Mol Biol Evol* 24, 1596-1599 (2007).
41. Thierry-Mieg, D. & Thierry-Mieg, J. AceView: a comprehensive cDNA-supported gene and transcripts annotation. *Genome Biol* 7 Suppl 1, S12 11-14 (2006).
42. Nakayama, M., Kikuno, R. & Ohara, O. Protein-protein interactions between large proteins: two-hybrid screening using a functionally classified library composed of long cDNAs. *Genome Res* 12, 1773-1784 (2002).
43. Lamalice, L., Le Boeuf, F. & Huot, J. Endothelial cell migration during angiogenesis. *Circ Res* 100, 782-794 (2007).
44. Moissoglu, K. & Schwartz, M.A. Integrin signalling in directed cell migration. *Biol Cell* 98, 547-555 (2006).

45. Berrier, A.L. & Yamada, K.M. Cell-matrix adhesion. *J Cell Physiol* 213, 565-573 (2007).
46. Katz, B.Z. *et al.* Physical state of the extracellular matrix regulates the structure and molecular composition of cell-matrix adhesions. *Mol Biol Cell* 11, 1047-1060 (2000).
47. Gao, B., Saba, T.M. & Tsan, M.F. Role of alpha(v)beta(3)-integrin in TNF-alpha-induced endothelial cell migration. *Am J Physiol Cell Physiol* 283, C1196-1205 (2002).
48. Brown, M.C. & Turner, C.E. Paxillin: adapting to change. *Physiol Rev* 84, 1315-1339 (2004).
49. Hynes, R.O. Integrins: versatility, modulation, and signaling in cell adhesion. *Cell* 69, 11-25 (1992).
50. Hodivala-Dilke, K.M., Reynolds, A.R. & Reynolds, L.E. Integrins in angiogenesis: multitalented molecules in a balancing act. *Cell Tissue Res* 314, 131-144 (2003).
51. Kabir-Salmani, M. *et al.* Alphavbeta3 integrin signaling pathway is involved in insulin-like growth factor I-stimulated human extravillous trophoblast cell migration. *Endocrinology* 144, 1620-1630 (2003).
52. West, K.A. *et al.* The LD4 motif of paxillin regulates cell spreading and motility through an interaction with paxillin kinase linker (PKL). *J Cell Biol* 154, 161-176 (2001).
53. May, J.A. *et al.* GPIIb-IIIa antagonists cause rapid disaggregation of platelets pre-treated with cytochalasin D. Evidence that the stability of platelet aggregates depends on normal cytoskeletal assembly. *Platelets* 9, 227-232 (1998).
54. Zhang, P. *et al.* Pim-3 is expressed in endothelial cells and promotes vascular tube formation. *J Cell Physiol* 220, 82-90 (2009).
55. Wang, C.H. *et al.* Thrombospondin type I domain containing 7A (THSD7A) mediates endothelial cell migration and tube formation. *J Cell Physiol* 222, 685-694.
56. Kurz, H. Physiology of angiogenesis. *J Neurooncol* 50, 17-35 (2000).
57. Bedell, V.M. *et al.* roundabout4 is essential for angiogenesis in vivo. *Proc Natl Acad Sci U S A* 102, 6373-6378 (2005).
58. Lawson, N.D. & Weinstein, B.M. In vivo imaging of embryonic vascular development using transgenic zebrafish. *Dev Biol* 248, 307-318 (2002).
59. Leung, T. *et al.* Zebrafish G protein gamma2 is required for VEGF signaling during angiogenesis. *Blood* 108, 160-166 (2006).
60. Heisenberg, C.P. *et al.* Silberblick/Wnt11 mediates convergent extension

movements during zebrafish gastrulation. *Nature* 405, 76-81 (2000).

61. Kantor, D.B. *et al.* Semaphorin 5A is a bifunctional axon guidance cue regulated by heparan and chondroitin sulfate proteoglycans. *Neuron* 44, 961-975 (2004).
62. Hilario, J.D., Rodino-Klapac, L.R., Wang, C. & Beattie, C.E. Semaphorin 5A is a bifunctional axon guidance cue for axial motoneurons in vivo. *Dev Biol* (2008).
63. Artigiani, S. *et al.* Plexin-B3 is a functional receptor for semaphorin 5A. *EMBO Rep* 5, 710-714 (2004).
64. Mahler, J. & Driever, W. Expression of the zebrafish intermediate neurofilament Nestin in the developing nervous system and in neural proliferation zones at postembryonic stages. *BMC Dev Biol* 7, 89 (2007).
65. Vogelezang, M., Forster, U.B., Han, J., Ginsberg, M.H. & ffrench-Constant, C. Neurite outgrowth on a fibronectin isoform expressed during peripheral nerve regeneration is mediated by the interaction of paxillin with alpha4beta1 integrins. *BMC Neurosci* 8, 44 (2007).
66. Woo, S. & Gomez, T.M. Rac1 and RhoA promote neurite outgrowth through formation and stabilization of growth cone point contacts. *J Neurosci* 26, 1418-1428 (2006).
67. Hodivala-Dilke, K. alphavbeta3 integrin and angiogenesis: a moody integrin in a changing environment. *Curr Opin Cell Biol* 20, 514-519 (2008).
68. Brooks, P.C., Clark, R.A. & Cheresh, D.A. Requirement of vascular integrin alpha v beta 3 for angiogenesis. *Science* 264, 569-571 (1994).
69. Reynolds, L.E. *et al.* Enhanced pathological angiogenesis in mice lacking beta3 integrin or beta3 and beta5 integrins. *Nat Med* 8, 27-34 (2002).
70. Taverna, D., Crowley, D., Connolly, M., Bronson, R.T. & Hynes, R.O. A direct test of potential roles for beta3 and beta5 integrins in growth and metastasis of murine mammary carcinomas. *Cancer Res* 65, 10324-10329 (2005).
71. Kondo, A. *et al.* A new paxillin-binding protein, PAG3/Papalpha/KIAA0400, bearing an ADP-ribosylation factor GTPase-activating protein activity, is involved in paxillin recruitment to focal adhesions and cell migration. *Mol Biol Cell* 11, 1315-1327 (2000).
72. Uchida, H., Kondo, A., Yoshimura, Y., Mazaki, Y. & Sabe, H. PAG3/Papalpha/KIAA0400, a GTPase-activating protein for ADP-ribosylation factor (ARF), regulates ARF6 in Fcgamma receptor-mediated phagocytosis of macrophages. *J Exp Med* 193, 955-966 (2001).
73. Turner, C.E., West, K.A. & Brown, M.C. Paxillin-ARF GAP signaling and the

cytoskeleton. *Curr Opin Cell Biol* 13, 593-599 (2001).

74. Norman, J.C. *et al.* ARF1 mediates paxillin recruitment to focal adhesions and potentiates Rho-stimulated stress fiber formation in intact and permeabilized Swiss 3T3 fibroblasts. *J Cell Biol* 143, 1981-1995 (1998).
75. Boshans, R.L., Szanto, S., van Aelst, L. & D'Souza-Schorey, C. ADP-ribosylation factor 6 regulates actin cytoskeleton remodeling in coordination with Rac1 and RhoA. *Mol Cell Biol* 20, 3685-3694 (2000).
76. Young, G.D. & Murphy-Ullrich, J.E. The tryptophan-rich motifs of the thrombospondin type 1 repeats bind VLAL motifs in the latent transforming growth factor-beta complex. *J Biol Chem* 279, 47633-47642 (2004).
77. Ludbrook, S.B., Barry, S.T., Delves, C.J. & Horgan, C.M. The integrin alphavbeta3 is a receptor for the latency-associated peptides of transforming growth factors beta1 and beta3. *Biochem J* 369, 311-318 (2003).
78. Lee, Y.H. *et al.* Transforming growth factor-beta1 effects on endothelial monolayer permeability involve focal adhesion kinase/Src. *Am J Respir Cell Mol Biol* 37, 485-493 (2007).
79. Swerlick, R.A., Lee, K.H., Wick, T.M. & Lawley, T.J. Human dermal microvascular endothelial but not human umbilical vein endothelial cells express CD36 in vivo and in vitro. *J Immunol* 148, 78-83 (1992).
80. Siekmann, A.F. & Lawson, N.D. Notch signalling limits angiogenic cell behaviour in developing zebrafish arteries. *Nature* 445, 781-784 (2007).
81. Covassin, L.D., Villefranc, J.A., Kacergis, M.C., Weinstein, B.M. & Lawson, N.D. Distinct genetic interactions between multiple Vegf receptors are required for development of different blood vessel types in zebrafish. *Proc Natl Acad Sci U S A* 103, 6554-6559 (2006).

Appendix

Functional annotation of KRAS mutations in the pancreatic tumorigenesis using novel zebrafish models.
(Research trainee program in Johns Hopkins Medical School)

➢ Introduction

Pancreatic cancer is a highly aggressive cancer with an overall 5-year survival rate of less than 5% [1]. Due to indolent tumor growth, difficulty in visualization and lack of specific markers, diagnosis of pancreatic cancer is frequently established at an advanced stage. Treatment options for advanced pancreatic cancer have limited success, and targeting therapy is therefore a promising strategy.

Pancreatic cancer appears to develop from pancreatic epithelial cells with oncogenic KRAS mutations [2]. In human, over 90% of pancreatic ductal adenocarcinomas (PDAC) display KRAS mutation [3, 4]. In mice, KRAS mutation induces the progression and invasion of pancreatic intraepithelial neoplasia (PanIN), a known precursor of PDAC [5-8]. Tumorigenicity of different KRAS mutations varies in pancreatic tumors. For example, expression of $KRAS^{G12\underline{V}}$ point mutation in mouse embryonic cells of anciar/ centroacinar lineage can induce PanIN after 1-3 months, and progress to PDAC at the age of 12 month [7]. However, these adult mice are refractory to $KRAS^{G12\underline{V}}$ oncogenic activity, unless a chronic pancreatitis is introduced [7]. Intriguingly, when $KRAS^{G12\underline{D}}$ is expressed in acinar cell, the adult mice are able to develop PanIN without any chronic exocrine injury [8]. In addition, expression of $KRAS^{G12\underline{D}}$ throughout the mouse body causes embryonic letheal, and induces preneoplastic hyperplasia in lung and GI tract [9], while widespread $KRAS^{G12\underline{V}}$ expression fails to induce unscheduled proliferation and other

developmental defects for up to 8 month [10]. Taken together, it is proposed that KRAS$^{G12\underline{D}}$ mutation may be more aggressive than KRAS$^{G12\underline{V}}$ to induce pancreatic tumorigenesis.

Zebrafish is a vertebrate model system with several competitive advantages over other systems. Additionally, the physiological and pathological characteristics of zebrafish have been clearly and repeatedly demonstrated similar to human. For example, expression of mutated KRAS^{G12V} in zebrafish pancreatic progenitor cells induces pancreatic tumorigenesis with histologically similar to human pancreatic tumor, including the same nuclear atypia, haphazard gland arrangement, desmoplastic stromal response, and locally invasive behavior [11, 12]. Thus, the attributes that used zebrafish in developmental and genetic study, in combination with the new established carcinogenesis assay, make the zebrafish an attractive model system for cancer research.

This study aims to compare the oncogenic activity of KRAS$^{G12\underline{D}}$ vs. KRAS$^{G12\underline{V}}$ in pancreatic tumorigenesis by using zebrafish model for its pros of easily genetic modification and rapid screening scheme, by which is able to unravel the oncogens that cooperate with deregulated KRAS mutants and genetic changes in associated with distinct types of the oncogenic KRAS-expressing tumors.

➢ Results

New models of pancreatic cancer in zebrafish have been generated by using a Gal4-UAS system in this study. An eGFP-fused KRAS$^{G12\underline{\mathbf{V}}}$ or a mKO2-fused KRAS$^{G12\underline{\mathbf{D}}}$ was constructed downstream of UAS promoter, that was under the trans-regulation of Gal4 activator driven by *ptf1a* regulatory elements. By using Tol2 recombination technology, co-injection of the UAS: eGFP- KRAS^{G12V} and the UAS: mKO2- KRAS^{G12D} constructs into the zebrafish embryos on the genetic background of *ptf1a*:Gal4-VP16 was performed, by which allowed eGFP- KRAS^{G12V} and mKO2-KRAS^{G12D} expression in exocrine pancreas. In order to avoid the concern that fused fluorescent protein may interfere the KRAS activities, another set of constructs were made in an opposite way and co-injected, i. e. UAS: eGFP- KRAS$^{G12\underline{\mathbf{D}}}$ and UAS: mKO2- KRAS$^{G12\underline{\mathbf{V}}}$ (Fig. I). Examination of living fish of Tg(ptf1a: Gal4-VP16; UAS: eGFP-KRAS^{G12V}; UAS:mKO2-KRAS^{G12D}) and Tg(ptf1a: Gal4-VP16; UAS: eGFP-KRAS^{G12D}; UAS:mKO2-KRAS^{G12V}) showed fluorescent expression in retina, hindbrain, spinal interneurons, and pancreas. This pattern recapitulated the reported expression of endogenous ptf1a, and the previously described Tg(*ptf1a*:eGFP) transgenic fish [12-15].

The F0 generation with double positive for both KRAS^{G12D} and KRAS^{G12V} expression were selected and raised, till tumor cells were observed based on its transcutaneous fluorescence or up to 5 months. Total 26 of F0 injected fish were examined, among which 46% developed tumors that expressed oncogenic KRAS mutations (Fig. II). Notably, KRAS^{G12D}-expressing cells were found more frequently than KRAS^{G12V} cells in these neoplastic tumor masses (Table I). 50.0% of examined tumor masses had KRAS^{G12D} expression, and 16.7% expressed KRAS^{G12V}. Additionally, 33.3% of tumor masses showed both KRAS^{G12D} and KRAS^{G12V} positive, among which KRAS^{G12D} expression was still dominant than KRAS^{G12V} within the

same tumor (Fig. II D, E). Interestingly, KRAS^{G12D}-positive cells were still capable of expressing KRAS^{G12V} (Fig. III A-C). It was also found KRAS^{G12D} and KRAS^{G12V} positive in distinct cell groups within the same tumor mass (Fig. III D-F). Histological examination revealed that these neoplastic cells displayed transformation similar to human pancreatic cancer, including acinar differentiation, ductal differentiation, mucinous differentiation, and a mixed characteristic (Table I; Fig. IV). These finding suggest the genetic regulations in oncogenic KRAS-induced pancreatic tumor are conserved among the vertebrates, and support the hypothesis that oncogenic KRAS$^{G12\underline{D}}$ is more aggressive than KRAS$^{G12\underline{V}}$ to induce pancreatic tumorigenesis in zebrafish.

- **Future Works**

The KRAS protein is a small GTPase, which becomes oncogenic by single point mutations, mainly at codon 12 and codon 13. Oncogenic KRAS leads to cell neoplastic transformation through constitute signaling that activates downstream effector pathways, including RAF-MEK-ERK pathway and PI3K/ Akt pathway [16]. Distinct signaling through different KRAS point mutations is found in the NIH3T3 fibroblasts. KRAS^{G12V} mutant interacts with Raf-1 and transduces signaling mainly through Erk pathway, while KRAS^{G12D} mutant involves PI3K/ Akt, JNK, and FAK pathways [17]. This difference maintains in the implanted mouse model of colorectal tumor [17]. Given the different aggressiveness of KRAS^{G12D} and KRAS^{G12V} to produce pancreatic tumors in our zebrafish model, it suggests that different genetic changes may occur in response to KRAS^{G12D} and KRAS^{G12V} in the progress of pancreatic tumorigenesis. The distinct genetic changes may also lead to different cell morphology, cell migration, proliferation, and apoptosis capacities,

resulting in different latency for tumor appearance and multiple tumor types. Besides, estimation of KRAS expression and its activity during tumor progress is required to study if the different disease latency of KRAS mutants is caused by their activated levels in triggering deregulated signaling pathway. Thus, $KRAS^{G12V}$ may need accumulation to the expression level before being capable of inducing tumorigenesis.

Given that pancreatic cancer usually presents clinically with malignant metastasis through neovasculature, it is interesting to note that the function of KRAS oncogene in tumor angiogenesis is poorly understood. Although Matsuo Y et. al. showed that $KRAS^{G12V}$ enhanced pancreatic tumor cells to produce angiogenic factors, including CXC chemokines and VEGF [18, 19]. Mechanism underlying the oncogenic KRAS-induced angiogenesis in pancreatic tumor is obscure. Additionally, treatment with bevacizumab (anti-VEGF monoclonal antibody) either alone or in combination with standard chemotherapy provides limited benefits in patients with advanced pancreatic cancer, leading to a doubt of broad-spectrum effects in the anti-angiogenic therapy. Also, it highlights an important role of tumor heterogeneity in antitumor therapy. The successful modeling of pancreatic tumorigenesis in zebrafish generates a novel platform for studies of novel angiogenic molecules with respect to oncogenic KRAS mutants in different tumor subtypes.

Given the high effectiveness of Tol2 transposon to introduce gene expression in zebrafish, the established fish models of KRAS-induced pancreatic cancer is able to study the genetic interactions that alternate KRAS tumorigenicity, including the tumor suppressor genes p53, cell cycle antigens p16, and novel oncogens such as PPDPF. In addition, the unique edge of zebrafish as a screening tool allows it being readily amenable to large-scale drug screening for antitumor therapy.

References

1. Whipple, C. & Korc, M. Targeting angiogenesis in pancreatic cancer: rationale and pitfalls. *Langenbecks Arch Surg* 393, 901-910 (2008).
2. Jones, S. *et al.* Core signaling pathways in human pancreatic cancers revealed by global genomic analyses. *Science* 321, 1801-1806 (2008).
3. Hruban, R.H. *et al.* K-ras oncogene activation in adenocarcinoma of the human pancreas. A study of 82 carcinomas using a combination of mutant-enriched polymerase chain reaction analysis and allele-specific oligonucleotide hybridization. *Am J Pathol* 143, 545-554 (1993).
4. Malumbres, M. & Barbacid, M. RAS oncogenes: the first 30 years. *Nat Rev Cancer* 3, 459-465 (2003).
5. Hruban, R.H. *et al.* Pathology of genetically engineered mouse models of pancreatic exocrine cancer: consensus report and recommendations. *Cancer Res* 66, 95-106 (2006).
6. Hingorani, S.R. *et al.* Preinvasive and invasive ductal pancreatic cancer and its early detection in the mouse. *Cancer Cell* 4, 437-450 (2003).
7. Guerra, C. *et al.* Chronic pancreatitis is essential for induction of pancreatic ductal adenocarcinoma by K-Ras oncogenes in adult mice. *Cancer Cell* 11, 291-302 (2007).
8. Habbe, N. *et al.* Spontaneous induction of murine pancreatic intraepithelial neoplasia (mPanIN) by acinar cell targeting of oncogenic Kras in adult mice. *Proc Natl Acad Sci U S A* 105, 18913-18918 (2008).
9. Tuveson, D.A. *et al.* Endogenous oncogenic K-ras(G12D) stimulates proliferation and widespread neoplastic and developmental defects. *Cancer Cell* 5, 375-387 (2004).
10. Guerra, C. *et al.* Tumor induction by an endogenous K-ras oncogene is highly dependent on cellular context. *Cancer Cell* 4, 111-120 (2003).
11. Stern, H.M. & Zon, L.I. Cancer genetics and drug discovery in the zebrafish. *Nat Rev Cancer* 3, 533-539 (2003).
12. Park, S.W. *et al.* Oncogenic KRAS induces progenitor cell expansion and malignant transformation in zebrafish exocrine pancreas. *Gastroenterology* 134, 2080-2090 (2008).
13. Esni, F. *et al.* Notch inhibits Ptf1 function and acinar cell differentiation in developing mouse and zebrafish pancreas. *Development* 131, 4213-4224 (2004).
14. Lin, J.W. *et al.* Differential requirement for ptf1a in endocrine and exocrine lineages of developing zebrafish pancreas. *Dev Biol* 270, 474-486 (2004).
15. Zecchin, E. *et al.* Evolutionary conserved role of ptf1a in the specification of exocrine pancreatic fates. *Dev Biol* 268, 174-184 (2004).
16. Vakiani, E. & Solit, D.B. KRAS and BRAF: drug targets and predictive biomarkers. *J*

Pathol 223, 219-229 (2010).

17. Cespedes, M.V. *et al.* K-ras Asp12 mutant neither interacts with Raf, nor signals through Erk and is less tumorigenic than K-ras Val12. *Carcinogenesis* 27, 2190-2200 (2006).
18. Matsuo, Y. *et al.* K-Ras promotes angiogenesis mediated by immortalized human pancreatic epithelial cells through mitogen-activated protein kinase signaling pathways. *Mol Cancer Res* 7, 799-808 (2009).
19. Matsuo, Y. *et al.* CXC-chemokine/CXCR2 biological axis promotes angiogenesis in vitro and in vivo in pancreatic cancer. *Int J Cancer* 125, 1027-1037 (2009).

TSING HUA UNIVERSITY

Table 1. Histological examination of pancreatic tumor masses. 12 out of 26 fish developed KRAS-positive tumors.

#	Age at sacrifice (months)	Histology	Oncogene expression		Accumulated percentage (Total # of fish: 26)
			eGFP	mKO	
1	2	Acinar differentiation	KrasG12D	KrasG12V	3.8%
2	3	Acinar differentiation	–	KrasG12V	11.5%
3	3	Mixed acinar & ductal differentiation	–	KrasG12D	11.5%
4	4	Mucinous differentiation	KrasG12V	–	23.0%
5	4	Acinar differentiation	–	KrasG12D	23.0%
6	4	Acinar differentiation	–	KrasG12D	23.0%
7	5	Mucinous differentiation	KrasG12D	KrasG12V	42.3%
8	5	Acinar differentiation	–	KrasG12D	42.3%
9	5	Acinar differentiation	KrasG12D	KrasG12V	42.3%
10	5	Acinar differentiation	–	KrasG12D	42.3%
11	5	Acinar differentiation	–	KrasG12D	42.3%
12	6	Acinar differentiation	KrasG12D	KrasG12V	46.2%

Figures and Tables

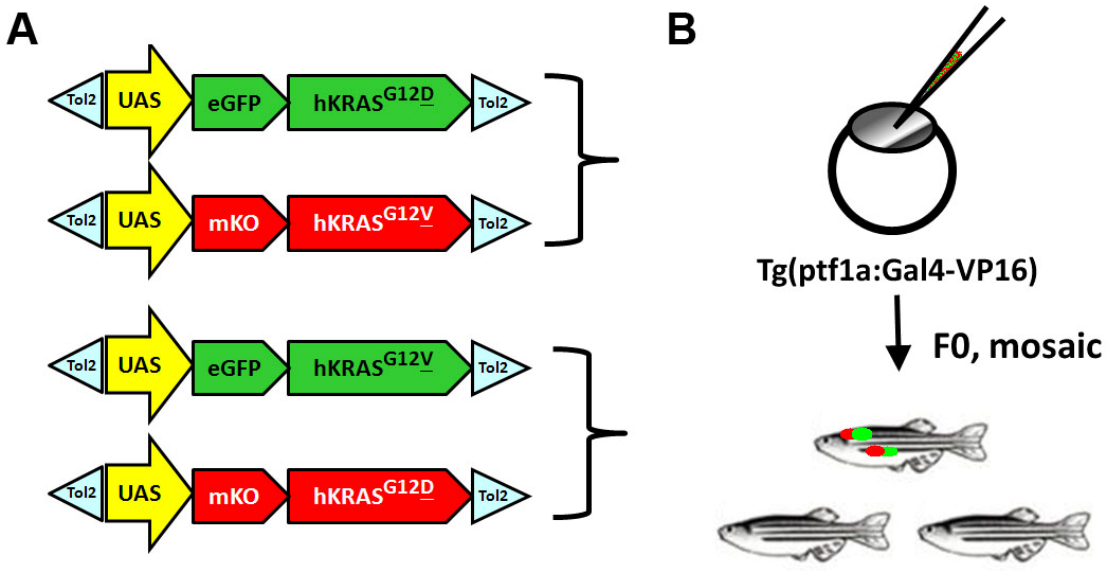

Fig. I. Scheme of experimental design. KRAS^{G12D} and KRAS^{G12V} were co-expressed in zebrafish by using a Gal4-UAS system. (A) Two sets of eGFP and mKO fluorescent protein-fused KRAS^{G12D} and KRAS^{G12V} were constructed downstream of UAS promoter in Tol2-based expression vectors. (B) Each set of constructs was injected into the embryos on genetic background of *ptf1a*: Gal4-VP16. F0 embryos with double positive for KRAS^{G12D} and KRAS^{G12V} in pancreas were raised up, and subjected to subsequent experiments.

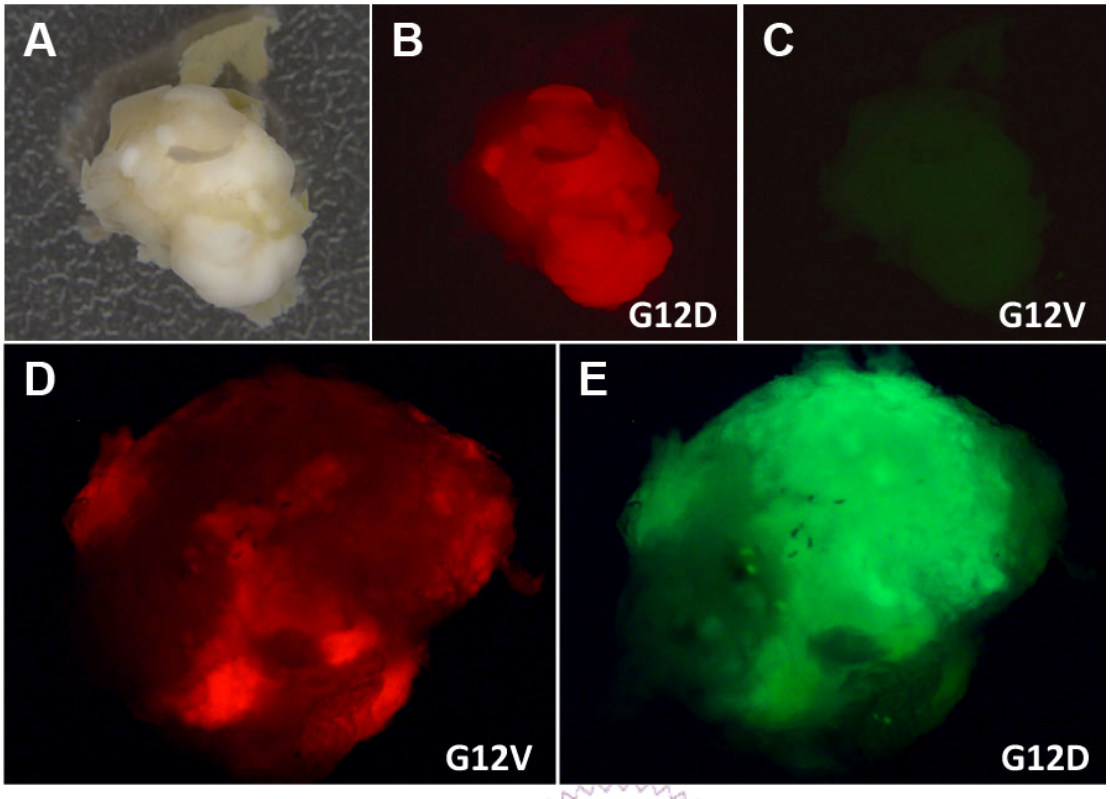

Fig. II. Pancreatic tumors were developed in oncogenic KRAS-expressing zebrafish. Neoplastic transformation of cells expressed oncogenic KRAS mutations. (A-C) A representative tumor mass showed KRAS^{G12D} positive, but not KRAS^{G12V}. (A) bright-field view of tumor mass. (B) Tumor cells that expressed mKO-KRAS^{G12D} were shown in red. (C) None of tumor cells was positive for eGFP fused KRAS^{G12V} (green). (D, E) A representative tumor mass expressed both KRAS^{G12V} and KRAS^{G12D}. Note that KRAS^{G12D} cells were dominant. (D) KRAS^{G12V}-positive cells were shown in red. (E) KRAS^{G12D}-positive cells were shown in green.

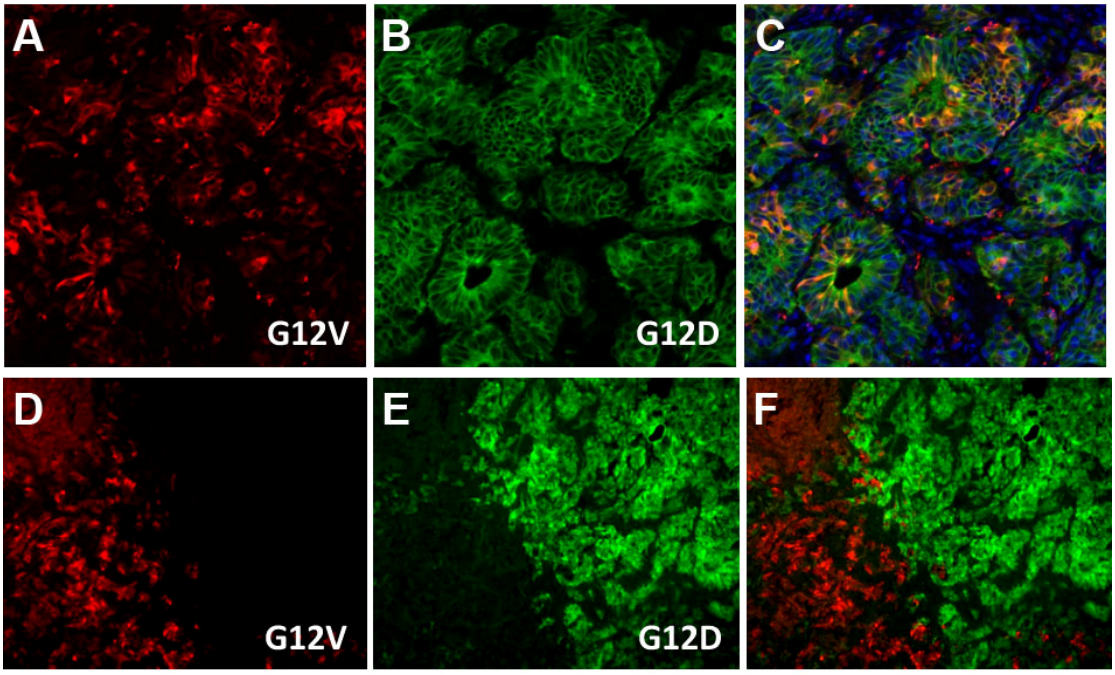

Fig. III. Tumor cells expressed both KRAS^{G12V} and KRAS^{G12D}. (A-C) Representative images showing tumor cells that expressed both KRAS^{G12V} (A) and KRAS^{G12D} (B). (C) Merged images of panel A and B. (D-F) Distinct cell group expressed either KRAS^{G12V} (D) or KRAS^{G12D} (E). (F) Merged image of panel D and E.

TSING HUA UNIVERSITY

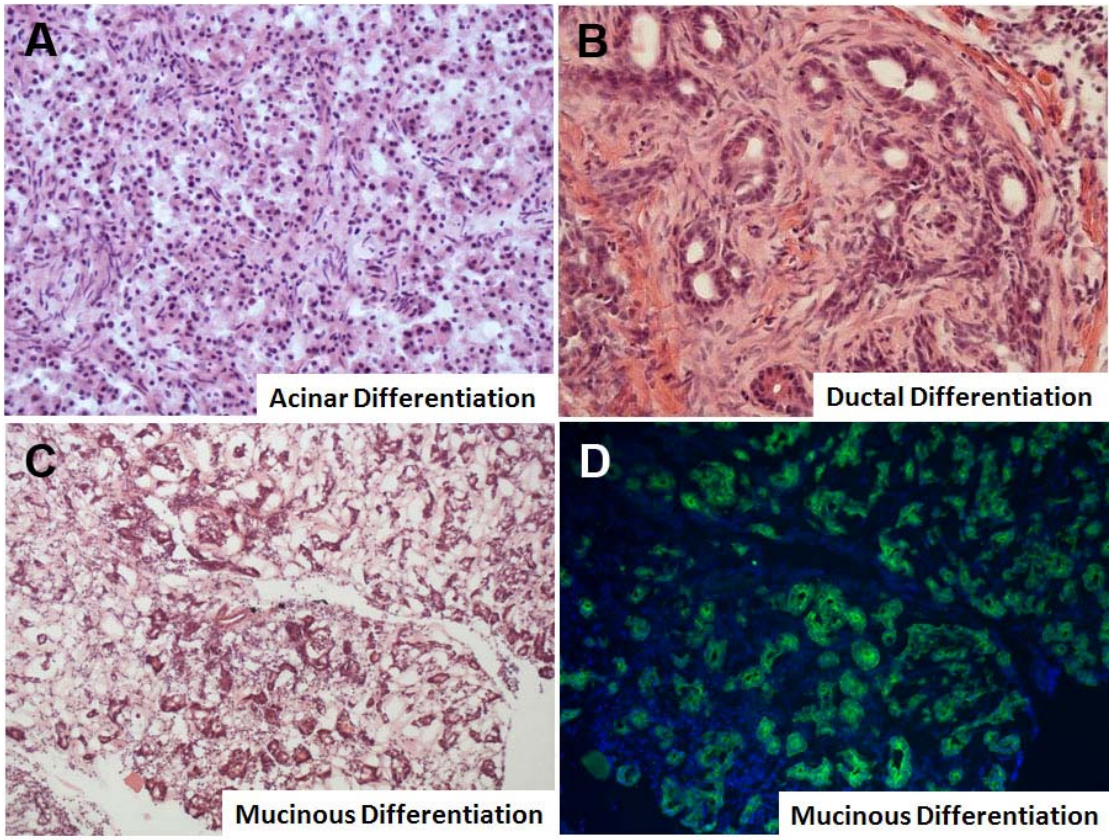

Fig. IV. Multiple types of neoplastic transformation were induced by KRAS mutants. Each tumor mass was sectioned and histological examined by H&E staining. Representative images showed acinar differentiation (A), ductal differentiation (B), and mucinous differentiation (C). (D) A serial section of mucinous-differentiated tumor showed $KRAS^{G12V}$-positive cells (green). Cell nuclei were stained by DAPI (blue).